

HESSIAN-FREE RAY-BORN INVERSION FOR QUANTITATIVE ULTRASOUND TOMOGRAPHY

ASHKAN JAVAHERIAN

*School of Electrical and Computer Engineering, University College of Engineering, University of
Tehran, Tehran, Iran.**

ABSTRACT. This study introduces a frequency-domain, Hessian-free ray-Born inversion method for quantitative ultrasound tomography, building upon the Hessian-based approach presented in our previous work. Both methods model acoustic wave propagation using a ray-based approximation of the heterogeneous Green's function and iteratively solve the inverse problem in the frequency domain, progressing from low to high frequencies. In the previous study, each frequency subproblem is solved by iterative inversion of the Hessian matrix, which significantly increases computational costs. The present study addresses this limitation by diagonalizing the Hessian matrix through specific weighting, enabling a single-step inversion for each subproblem. This modification reduces computational expense by approximately an order of magnitude compared to the Hessian-based method, bringing its efficiency in line with radon-type, time-of-flight-based methods that use bent rays. Furthermore, by incorporating regularization directly into the forward operator and balancing computational efficiency with spatial resolution, the Hessian-free method achieves robust image reconstructions that are less sensitive to noise and inaccuracies in the initial model. For the ray-based approximation, this study introduces a paraxial ray-tracing system. Instead of independently tracing an auxiliary ray, the Jacobian of the ray is approximated by simultaneously tracing a paraxial ray alongside the linked ray. This approach improves computational efficiency while maintaining accuracy.

1. INTRODUCTION

Ultrasound tomography (UST) is a technique used to map the acoustic properties of an object based on ultrasonic excitations and measurements taken from outside the object [2]. This method has gained significant interest in biomedical applications, particularly for detecting malignant tumors in the breast [3]. Ideally, ultrasound data provides quantitative distributions of sound speed, absorption, and density, as well as a qualitative map of reflectivity [4, 5, 6]. This manuscript specifically focuses on sound speed reconstruction, and thus, the term UST will refer to this process [7]. Approaches for sound speed imaging in UST can be categorized based on: (1) the type of data used in inversion, (2) whether the objective function to be minimized is nonlinear or linearized, (3) whether the objective function is defined in the time or frequency domain, and (4) the forward model employed.

E-mail address: ashkan.javaherian@ut.ac.ir.

Date: First version: November 2022; Last update: December 2024.

*This work was predominantly conducted at the Department of Medical Physics and Biomedical Engineering, University College London, UK, during the author's employment there. Subsequent refinements and revisions were completed at the University of Tehran.

Ashkan Javaherian, Ray-based quantitative-ultrasound tomography toolbox, 2022, <https://github.com/Ash1362/ray-based-quantitative-ultrasound-tomography/>

The first class of approaches relies exclusively on direct times-of-flight data between emitters and receivers, effectively ignoring scattered waves [8, 9]. The second class incorporates the full time-series data, including scattered waves, to provide a more comprehensive representation of the medium [10, 11, 12, 13, 14]. The third class strikes a balance by leveraging direct arrivals and primarily scattered waves, offering improved accuracy compared to the first class while maintaining a reduced computational burden relative to the second class [15, 16, 17, 18, 19, 20, 21, 22, 23, 24, 25]. This study adopts a hybrid approach that leverages the strengths of both the first and third classes: direct times-of-flight data are utilized to generate an initial estimate, while predominantly scattered waves are iteratively incorporated to refine the solution to the main inverse problem. We solve this problem using an iterative linearization of the objective function, with linearizations performed in the frequency domain, progressing from low to high frequencies. The forward problem is modeled using a ray-approximation to heterogeneous Green’s functions. Ray theory, based on a high-frequency approximation, strikes a balance between accuracy and computational efficiency for broadband data [26]. While ray theory has limitations in seismic imaging, such as caustics and multivaluedness of minimal acoustic length [27], these challenges are less critical for imaging soft tissues, like the breast, where the refractive index typically ranges from 0.9 to 1.1.

The main challenges in extending high-resolution quantitative ultrasound to 3D imaging via full-wave inversion are computational cost and transducer directivity, both of which can be managed more easily with ray-based methods [1]. Previous work demonstrated numerically that ray-based methods for UST can reconstruct high-resolution sound speed maps with significantly lower computational cost compared to full-wave inversion methods that solve the wave equation in its entirety [12, 14].

Common methods accounting for diffraction or singly scattered waves typically rely on the Green’s function in a homogeneous medium, incorporating acoustic heterogeneity only within the scattering potential [15, 16, 17, 18, 19, 20, 21, 23, 24, 25]. However, it has been shown that combining ray theory with Born inversion can significantly improve accuracy by incorporating sound speed heterogeneity, refraction, and acoustic absorption and dispersion into the Green’s functions that predict incident and scattered waves [1]. A one-step inversion method combining diffraction tomography with ray tracing was proposed in [28], which compensates for phase aberrations in the Green’s function due to heterogeneities by performing ray tracing on a low-resolution image, initially reconstructed using a time-of-flight-based method, and solving the inverse problem in a single step.

Using a forward model based on the ray approximation, the Green’s functions are approximated along rays initialized at the emitters and intercepted by the receivers after traversing the medium, referred to as linked rays. While the phases and the acoustic absorption components of the amplitudes are approximated along the linked rays, computing the geometrical components of the amplitudes requires evaluating the rays’ Jacobian, which traditionally involves tracing an auxiliary ray for each linked ray. In [1], the auxiliary rays are traced independently of the linked rays by introducing small perturbations to the initial angles of the linked rays. In contrast, this study introduces a paraxial ray-tracing system, where a paraxial ray is traced simultaneously with the linked ray. This approach enhances both efficiency and stability in computing the rays’ Jacobian. The UST inversion approaches proposed in [1] and extended in this study belong to the class of linearized inversion techniques known as ray-Born migration/inversion in inverse seismic theory [26, 29, 30, 31]. In [1], the objective function is discretized in the frequency domain, linearized, and sequentially minimized across the frequency range spanned by the ultrasound transducers. The frequency range is divided into intervals, each containing a fixed number of discretized frequencies (two in this case). Minimization proceeds sequentially, starting with the low-frequency intervals.

The solution from each subproblem serves as the initial guess for the next frequency set. Since reconstructing acoustic parameters from ultrasound data is a nonlinear inverse problem, minimizing the objective function from low to high frequencies helps avoid convergence to local minima [10, 11, 24].

Each linearized minimization subproblem in [1], which requires approximating the action of the inverse Hessian matrix on the gradient of the objective function, is solved using a Conjugate Gradient (CG) algorithm. This involves iterative computations of the Fréchet derivative of the forward operator and its adjoint. For each emitter-receiver pair, each CG iteration includes two-way forward propagation of Green’s functions from the emitter to the receiver, followed by two-way back-projection from the receiver to the emitter. These steps are repeated across all emitters, leading to significant computational costs. While the method in [1] incurs additional overhead from implicit inversion of the Hessian, it achieves a two-order-of-magnitude reduction in total computational time compared to the k-space pseudo-spectral approach for full-waveform inversion in 2D settings [32, 33, 34, 35].

The current manuscript aims to further reduce computational costs by introducing a single-step solution for each linearized subproblem. In this method, the Hessian matrix is diagonalized using a high-frequency approximation within the Born approximation framework. By assuming that primary scattering predominantly occurs near the ray connecting an emitter-receiver pair, the inversion process is simplified, reducing computational costs to levels comparable to time-of-flight-based inversion using bent rays [36]. This framework not only enhances computational efficiency but also serves as an implicit regularization mechanism, suppressing noise and artifacts while preserving fine scattering features essential for high-resolution imaging. Furthermore, the proposed method circumvents explicit Hessian computations, making it well-suited for large-scale applications, including high-resolution 3D imaging.

Section 2 introduces a Green’s function solution to the frequency-domain Helmholtz wave equation using ray theory, applicable to weakly heterogeneous and absorbing media. Section 3 details the Hessian-free ray-Born inversion approach for solving the inverse problem in UST. Section 4 discusses ray tracing and the approximation of the Green’s function for heterogeneous media using ray theory. Section 5 outlines the procedure for discretizing both the forward and inverse problems. Section 6 numerically validates the ray approximation to the heterogeneous Green’s function and presents reconstructed images demonstrating the performance of the proposed Hessian-free ray-Born inversion approach, compared to the more computationally expensive Hessian-based method from [1]. A discussion of these results follows in Section 7.

2. FORWARD PROBLEM

This section outlines the forward problem for reconstructing the spatially-varying sound speed. Let $\boldsymbol{x} = [x^1, \dots, x^d]^T$ denote a spatial position in \mathbb{R}^d , where d represents the number of spatial dimensions, typically 2 or 3. While this study focuses on the case $d = 2$, the findings aim to be extended to $d = 3$. To avoid repetition, this section is kept concise, and readers are directed to Section 3 of [1] for further details.

2.1. Problem setting. The domain $\Omega \subset \mathbb{R}^2$ is an open, bounded set containing the spatially-varying sound speed distribution $c(\boldsymbol{x})$. The variation is represented by $[c_0/c(\boldsymbol{x}) - 1] \in C_0^\infty$, where c_0 is the uniform sound speed outside Ω (e.g., the sound speed in water). The boundary of Ω is a circular ring $\mathbb{S} \subset \mathbb{R}$ containing the emission and reception elements, denoted by \bar{e} (emitter) and \bar{r} (receiver). These elements are modeled as point sources and detectors, respectively.

Each emitter $\bar{e} \in \{1, \dots, N_e\}$, centered at position e , is sequentially excited by a pulse acting as a source $s(t, e)$ over the time interval $t \in (0, T_s)$. The resulting acoustic pressure field propagates through the object immersed in water and is recorded by receivers $\bar{r} \in \{1, \dots, N_r\}$, centered at positions r , over the time interval $t \in (0, T)$, with $T \gg T_s$. For each emitter \bar{e} , the time-series data recorded by a receiver \bar{r} is denoted by $p(t, r, e)$.

The inverse problem is to reconstruct the spatial distribution $c(\mathbf{x})$ from the measured pressure time-series $p(t, r, e)$ for all emitter-receiver pairs, given the source $s(t, e)$.

While the measurements are typically made in the time domain using a broadband excitation signal, the image reconstruction is performed in the frequency domain. To facilitate this, the following Fourier transform pair is defined between the time and temporal frequency domains:

$$\hat{p}(\omega) = \mathcal{F}p(t) = \int_{-\infty}^{\infty} p(t)e^{i\omega t} dt, \quad p(t) = \mathcal{F}^{-1}\hat{p}(\omega) = \frac{1}{2\pi} \int_{-\infty}^{\infty} \hat{p}(\omega)e^{-i\omega t} d\omega. \quad (1)$$

2.2. Lossy Helmholtz Equation and Complex Wavevector. The propagation of a single-frequency acoustic pressure field, $\hat{p}(\omega, \mathbf{x})$, in an absorbing medium is governed by the lossy Helmholtz equation:

$$\left[\tilde{k}(\mathbf{x})^2 + \nabla^2 \right] \hat{p}(\omega, \mathbf{x}, e) = -s(\omega, e), \quad (2)$$

where $\tilde{k}(\mathbf{x})$ is the complex wavenumber, which can be chosen arbitrarily. In this study, the complex wavenumber is selected based on Szabo's absorption model, consistent with the absorption model used in the full-waveform solver for generating the synthetic ultrasound data benchmarked in Section 6 [35]. The associated complex wavenumber is given by [37]:

$$\begin{aligned} \tilde{k} &= \frac{\omega}{c} - \frac{\alpha_0(-i)^{y+1}\omega^y}{\cos(\pi y/2)} \\ &= \frac{\omega}{c} + \alpha \left[\tan\left(\frac{\pi y}{2}\right) + i \right] = k + i\alpha. \end{aligned} \quad (3)$$

By introducing $(-i)^y = \cos(\pi y/2) - i \sin(\pi y/2)$, the imaginary part represents the power-law absorption $\alpha = \alpha_0 \omega^y$, where α_0 has units of $\text{Np}(\text{rad/s})^{-y} \text{m}^{-1}$, and y is a non-integer power-law exponent, typically in the range $1 < y \leq 1.5$ for soft tissues [38, 39]. Furthermore, the real part k satisfies:

$$k = \frac{\omega}{c} + \alpha_0 \tan\left(\frac{\pi y}{2}\right) \omega^y = \frac{\omega}{c_p(\omega)}, \quad (4)$$

where $c_p(\omega)$ denotes the phase speed [37].

Additionally, the complex wavevector is defined as $\tilde{\mathbf{k}} = \mathbf{k} + i\mathbf{k}_i$, where:

$$|\mathbf{k}| = k, \quad \mathbf{k}_i = \frac{\alpha}{k} \mathbf{k}, \quad (5)$$

with $|\cdot|$ representing the L2 norm. Its relationship with the wavenumber is given by:

$$\tilde{\mathbf{k}} = \frac{\tilde{k}}{k} \mathbf{k}. \quad (6)$$

Here, the complex wavenumber \tilde{k} depends solely on the local acoustic properties of the medium at the position \mathbf{x} . In contrast, the wavevector \mathbf{k} is influenced by the wavenumber k along the entire ray path emanating from an emitter e (or receiver r) and passing through \mathbf{x} .

The Green's function solution to (2) is given by:

$$\hat{p}(\omega, \mathbf{x}) = \int g(\omega, \mathbf{x}, \mathbf{x}') s(\omega, \mathbf{x}') d\mathbf{x}', \quad (7)$$

where $g(\omega, \mathbf{x}, \mathbf{x}')$ satisfies the equation:

$$\left[\tilde{k}(\mathbf{x})^2 + \nabla^2 \right] g(\omega, \mathbf{x}, \mathbf{x}') = -\delta(\mathbf{x} - \mathbf{x}'). \quad (8)$$

For 2D settings in heterogeneous and absorbing media, the Green's function can be approximated as:

$$g(\omega, \mathbf{x}, \mathbf{x}') \approx A(\omega, \mathbf{x}, \mathbf{x}') \exp \left(i \left[\phi(\omega, \mathbf{x}, \mathbf{x}') + \frac{\pi}{4} \right] \right), \quad (9)$$

where ϕ is the phase, and $A = A_{abs} A_{geom}$ is the amplitude factor, incorporating contributions from absorption (A_{abs}) and geometric spreading (A_{geom}). Substituting (9) into (8), assuming $\alpha^2 \ll k^2$ and the high-frequency approximation $|\nabla^2 A/A| \ll k^2$, yields the Eikonal equation:

$$\nabla \phi \cdot \nabla \phi = k^2, \quad (10)$$

and the Transport equation:

$$\nabla \cdot \left[A_{geom}^2 \nabla \phi \right] = 0. \quad (11)$$

Further details on the derivation of these two equations are provided in Appendix A. Using the Eikonal equation (10), rays are trajectories perpendicular to surfaces of constant phase and are tangent to the real part of the complex wavevector, \mathbf{k} , satisfying:

$$\mathbf{k} = \nabla \phi. \quad (12)$$

The accumulated phase along a ray trajectory $\mathcal{C}(\mathbf{x}, \mathbf{x}')$ is:

$$\phi(\omega, \mathbf{x}, \mathbf{x}') = \exp \left(\int_{\mathcal{C}(\mathbf{x}, \mathbf{x}')} \mathbf{k} \cdot d\mathbf{x} \right), \quad (13)$$

and the absorption contribution to the amplitude is:

$$A_{abs}(\omega, \mathbf{x}, \mathbf{x}') = \exp \left(- \int_{\mathcal{C}(\mathbf{x}, \mathbf{x}')} \mathbf{k}_i \cdot d\mathbf{x} \right). \quad (14)$$

The geometric spreading term A_{geom} is determined using the Transport equation (11) and satisfies:

$$A_{geom}(\omega, \mathbf{x}, \mathbf{x}') = \left[\frac{S(\omega, \mathbf{x}') \rho(\mathbf{x}) c(\mathbf{x})}{S(\omega, \mathbf{x}) \rho(\mathbf{x}') c(\mathbf{x}')} \right]^{1/2}, \quad (15)$$

where ρ is the medium density (assumed homogeneous, $\rho(\mathbf{x}) = \rho(\mathbf{x}')$), and $S(\mathbf{x})$ is the ray tube area. At the initial point \mathbf{x}_0 of a ray, the geometric amplitude $A_{geom}(\mathbf{x}, \mathbf{x}_0)$ vanishes because the ray tube area is zero at \mathbf{x}_0 [27]. To avoid this, a reference point \mathbf{x}_{ref} is chosen near \mathbf{x}_0 , where $|\mathbf{x}_{ref} - \mathbf{x}_0| < \epsilon$, with ϵ being a small neighborhood radius in which the medium is homogeneous. The geometric amplitude at the reference point is expressed as:

$$A_{geom}(\omega, \mathbf{x}_{ref}, \mathbf{x}_0) = [8\pi \phi_0(\omega, \mathbf{x}_{ref}, \mathbf{x}_0)]^{-1/2}, \quad (16)$$

where $\phi_0(\omega, \mathbf{x}_{ref}, \mathbf{x}_0) = k_0 |\mathbf{x}_{ref} - \mathbf{x}_0|$, and $k_0 = \omega/c_0$ represents the wavenumber in water.

The geometric amplitude at an arbitrary point along the ray is then:

$$A_{geom}(\omega, \mathbf{x}, \mathbf{x}_0) = A_{geom}(\omega, \mathbf{x}_{ref}, \mathbf{x}_0) A_{geom}(\omega, \mathbf{x}, \mathbf{x}_{ref}), \quad (17)$$

where $A_{geom}(\omega, \mathbf{x}, \mathbf{x}_{ref})$ is computed using (15) with $\mathbf{x}' = \mathbf{x}_{ref}$.

3. INVERSE PROBLEM

This section presents the proposed approach for solving the nonlinear inverse problem in ultrasound tomography (UST), which involves reconstructing the sound speed distribution c of an object from pressure time series $p(t, r, e)$. These measurements are obtained through sequential excitations and recordings conducted with an array of ultrasound transducers encircling the object. Following [1], the associated objective function is linearized at multiple discretized frequencies within the operational range of the transducers. The linearized subproblems are solved in a sequential manner, starting from low frequencies and progressing to higher ones. At each step, the solution from the current frequency set serves as the initial guess for solving the next subproblem. In its standard form, each linearized subproblem requires evaluating the product of the inverse of the Hessian matrix with the gradient of the objective function. This can be achieved iteratively by computing products of the Hessian with perturbations to the unknown parameter, the sound speed, until a perturbation is found that minimizes the linearized objective function [1]. As an alternative to this iterative approach, the current study introduces weighting in both the data and solution spaces to diagonalize the Hessian matrix. This adjustment allows the matrix to be inverted in a single step, significantly simplifying the solution of each linearized subproblem.

In [1], the objective function was minimized with respect to the sound speed c . In contrast, this study minimizes the objective function with respect to the squared slowness $m = c^{-2}$, to facilitate the diagonalization of the Hessian matrix. Accordingly, a weighted objective function is formulated in terms of the Green's function in the frequency domain:

$$\mathcal{F}(m) = \frac{1}{2} \sum_{e,r} \int g_{\text{res}}(m; \omega, r, e)^* \mathcal{Q}_g(m; \omega, r, e) g_{\text{res}}(m; \omega, r, e) d\omega, \quad (18)$$

where $*$ denotes the complex conjugate, and $\mathcal{Q}_g(m; \omega, r, e)$ is a diagonal weighting matrix component in the data space (ω, r, e) . (The derivation of \mathcal{Q}_g will follow.) The term g_{res} represents the *residual*, defined as

$$g_{\text{res}}(m; \omega, r, e) = g(m; \omega, r, e) - \hat{g}(\omega, r, e), \quad (19)$$

where $g(m; \omega, r, e)$ and $\hat{g}(\omega, r, e)$ denote the *approximated* and *measured* Green's functions, respectively, at frequency ω , receiver position r , and emitter position e . The measured Green's function $\hat{g}(\omega, r, e)$ is obtained by deconvolving the source $s(\omega, e)$ from the measured pressure $\hat{p}(\omega, r, e)$ in the frequency domain. (An analogous formulation can be applied directly to an objective function based on pressure data, as in [1].)

3.1. Linearized objective function. Linearizing the objective function (18) about the squared slowness $m^{(n)}$, where n represents the number of linearization steps, yields:

$$\delta m^{(n)} \approx \arg \min_{\delta m} \frac{1}{2} \sum_{e,r} \int \left[\left[\delta g^{(n)}(\omega, r, e) [\delta m] + g_{\text{res}}^{(n)}(\omega, r, e) \right]^* \mathcal{Q}_g^{(n)}(\omega, r, e) \right. \\ \left. \left[\delta g^{(n)}(\omega, r, e) [\delta m] + g_{\text{res}}^{(n)}(\omega, r, e) \right] \right] d\omega, \quad (20)$$

where the notations $\mathcal{Q}_g^{(n)}(\omega, r, e) = \mathcal{Q}_g(m^{(n)}; \omega, r, e)$ and $g_{\text{res}}^{(n)}(\omega, r, e) = g_{\text{res}}(m^{(n)}; \omega, r, e)$ are defined for brevity. This linearized minimization subproblem seeks a perturbation $\delta m^{(n)}$ that adjusts the perturbed Green's function to match the residual. The perturbed Green's function $\delta g^{(n)}(\omega, r, e) [\delta m]$

is expressed as:

$$\delta g^{(n)}(\omega, r, e)[\delta m] = \int \frac{\partial g^{(n)}(\omega, r, e)}{\partial m^{(n)}(\mathbf{x}')} \delta m(\mathbf{x}') d\mathbf{x}', \quad (21)$$

where $g^{(n)}(\omega, r, e) = g(m^{(n)}; \omega, r, e)$ and $\frac{\partial g^{(n)}(\omega, r, e)}{\partial m^{(n)}(\mathbf{x}'')}$ is the Fréchet derivative of the Green's function with respect to m at \mathbf{x}' . This derivative satisfies:

$$\frac{\partial g^{(n)}(\omega, r, e)}{\partial m^{(n)}(\mathbf{x}')} = g^{(n)}(\omega, r, \mathbf{x}') \Upsilon_m^{(n)}(\omega, \mathbf{x}') g^{(n)}(\omega, \mathbf{x}', e), \quad (22)$$

where $\Upsilon_m^{(n)}(\omega, \mathbf{x}')$ represents the scattering potential:

$$\Upsilon_m^{(n)}(\omega, \mathbf{x}') = \Upsilon_c^{(n)}(\omega, \mathbf{x}') \frac{\partial c(\mathbf{x}')}{\partial m(\mathbf{x}')} = \omega c^{(n)}(\mathbf{x}') \tilde{k}^{(n)}(\mathbf{x}'), \quad (23)$$

and $\tilde{k}^{(n)}$ satisfies Eq. (3) for $c^{(n)}$ and α , assumed fixed with respect to n (see [1], Section 4.1, for further derivations).

3.2. Weighted Gradient and Hessian. The linearized subproblem is equivalent to solving:

$$\nabla \mathcal{F}^{(n)}(\mathbf{x}) + \int H^{(n)}(\mathbf{x}, \mathbf{x}') \delta m(\mathbf{x}') d\mathbf{x}' = 0, \quad (24)$$

where $\nabla \mathcal{F}^{(n)}$ is the functional gradient, weighted in both data and solution spaces:

$$\nabla \mathcal{F}^{(n)}(\mathbf{x}) = \sum_{e,r} \int \mathcal{Q}_m^{(n)}(\mathbf{x}) \left[\frac{\partial g^{(n)}(\omega, r, e)}{\partial m^{(n)}(\mathbf{x})} \right]^* \mathcal{Q}_g^{(n)}(\omega, r, e) g_{\text{res}}^{(n)}(\omega, r, e) d\omega. \quad (25)$$

The Hessian matrix's action, weighted similarly, is:

$$H^{(n)}(\mathbf{x}, \cdot) \delta m = \sum_{e,r} \int \mathcal{Q}_m^{(n)}(\mathbf{x}) \left[\frac{\partial g^{(n)}(\omega, r, e)}{\partial m^{(n)}(\mathbf{x})} \right]^* \mathcal{Q}_g^{(n)}(\omega, r, e) \delta g^{(n)}(\omega, r, e)[\delta m] d\omega. \quad (26)$$

Substituting further yields the weighted Hessian:

$$H^{(n)}(\mathbf{x}, \mathbf{x}') = \sum_{e,r} \int \mathcal{Q}^{(n)}(\omega, r, e, \mathbf{x}) \mathcal{D}^{(n)}(\omega, r, e, \mathbf{x}, \mathbf{x}') e^{-i\Phi^{(n)}(\omega, r, e, \mathbf{x}, \mathbf{x}')} d\omega, \quad (27)$$

where

$$\mathcal{Q}^{(n)}(\omega, r, e, \mathbf{x}) = \mathcal{Q}_m^{(n)}(\mathbf{x}) \mathcal{Q}_g^{(n)}(\omega, r, e). \quad (28)$$

Additionally, $\mathcal{D}^{(n)}$ and $\Phi^{(n)}$ are defined as:

$$\begin{aligned} \mathcal{D}^{(n)}(\omega, r, e, \mathbf{x}, \mathbf{x}') &= \left[A^{(n)}(\omega, r, \mathbf{x}) \Upsilon_m^{(n)}(\omega, \mathbf{x}) A^{(n)}(\omega, \mathbf{x}, e) \right]^* \left[A^{(n)}(\omega, r, \mathbf{x}') \Upsilon_m^{(n)}(\omega, \mathbf{x}') A^{(n)}(\omega, \mathbf{x}', e) \right], \\ \Phi^{(n)}(\omega, r, e, \mathbf{x}, \mathbf{x}') &= \phi^{(n)}(\omega, r, \mathbf{x}) + \phi^{(n)}(\omega, \mathbf{x}, e) - [\phi(\omega, r, \mathbf{x}') + \phi(\omega, \mathbf{x}', e)]. \end{aligned} \quad (29)$$

3.3. Diagonalized Hessian. The Hessian diagonalization relies on two approximations applied to (27), as proposed in [26, 29, 30, 31]:

$$\mathcal{D}^{(n)}(\omega, r, e, \mathbf{x}, \mathbf{x}') \approx \mathcal{D}^{(n)}(\omega, r, e, \mathbf{x}', \mathbf{x}'), \quad (30)$$

and

$$\begin{aligned} \Phi^{(n)}(\omega, r, e, \mathbf{x}, \mathbf{x}') &\approx \nabla_{\mathbf{x}'} \left(\phi^{(n)}(\omega, r, \mathbf{x}') + \phi^{(n)}(\omega, \mathbf{x}', e) \right) \cdot (\mathbf{x} - \mathbf{x}') \\ &= \bar{\mathbf{k}}^{(n)}(\omega, r, e, \mathbf{x}') \cdot (\mathbf{x} - \mathbf{x}'), \end{aligned} \quad (31)$$

where $\bar{\mathbf{k}}^{(n)}(\omega, r, e, \mathbf{x}')$ represents the gradient of a two-way isochron—a curve in the scattering point space \mathbf{x}' where the sum of the accumulated phase from the emitter position e to the scatterer \mathbf{x}' and from \mathbf{x}' to the receiver r is constant [29, 30].

Thus, $\bar{\mathbf{k}}^{(n)}(\omega, r, e, \mathbf{x}')$ is a vector passing through \mathbf{x}' and normal to the two-way isochron, given by:

$$\bar{\mathbf{k}}(\omega, r, e, \mathbf{x}') = \mathbf{k}(\omega, \mathbf{x}', e) + \mathbf{k}(\omega, r, \mathbf{x}') = \mathbf{k}(\omega, \mathbf{x}', e) - \mathbf{k}(\omega, \mathbf{x}', r),$$

with $\mathbf{k}(\omega, \mathbf{x}', e) = \nabla_{\mathbf{x}'} \phi(\omega, \mathbf{x}', e)$ and $\mathbf{k}(\omega, \mathbf{x}', r) = \nabla_{\mathbf{x}'} \phi(\omega, \mathbf{x}', r)$ representing the wavevectors of rays emanating from e and r , respectively, at \mathbf{x}' . In the polar coordinates, the wavevectors \mathbf{k} are represented by the pairs (k, γ) .

For a sufficiently smooth wavenumber field k , the contributions of emitter e and receiver r to the Hessian $H(\mathbf{x}, \mathbf{x}')$ decay as one moves away from the ray connecting e and r , particularly along planes perpendicular to the ray. This is because the phase function $\Phi^{(n)}(\omega, r, e, \mathbf{x}, \mathbf{x}')$ oscillates, and $\mathcal{D}^{(n)}(\omega, r, e, \mathbf{x}, \mathbf{x}')$ decreases in magnitude.

In ray theory, the region around a ray linking e and r that contributes to the wavefield at r is known as the Fresnel volume. A point \mathbf{x} belongs to the Fresnel volume corresponding to a ray linking e and r at frequency ω if the accumulated phase discrepancy satisfies:

$$|\phi(\omega, r, \mathbf{x}) + \phi(\omega, \mathbf{x}, e) - \phi(\omega, r, e)| < \pi. \quad (32)$$

For more details, see [27], Section 3.1.6. Assuming no caustics along the rays, only points near the ray linking e and r satisfy (32). This assumption is valid for soft tissues. The approximation (31) implies that the two-way accumulated phase associated with \mathbf{x} can be approximated by a Taylor expansion about \mathbf{x}' , neglecting higher-order terms. Similarly, (30) assumes:

$$A(\omega, r, \mathbf{x}) \Upsilon_m(\omega, \mathbf{x}) A(\omega, \mathbf{x}, e) \approx A(\omega, r, \mathbf{x}') \Upsilon_m(\omega, \mathbf{x}') A(\omega, \mathbf{x}', e). \quad (33)$$

This approximation relies on two assumptions:

- (1) The two-way attenuation from e to r is approximately constant within the Fresnel volume.
- (2) Variations in $\alpha_0 c \omega^{y-1}$ within the medium are negligible (e.g., in soft tissues like the breast).

For instance, in soft tissues such as the breast, consider a sound speed of 1500 m/s, an absorption coefficient $\alpha_0 = 0.5$ dB MHz^{-y} cm⁻¹ (equivalent to 1.75×10^{-9} Np(rad/s)^{-y} m⁻¹), and a frequency of 1 MHz. Under these conditions, the parameter $\alpha_0 c \omega^{(y-1)}$ evaluates to approximately 6.6×10^{-4} Np/rad. This small value demonstrates that variations in the medium's properties, specifically $\alpha_0 c \omega^{(y-1)}$, are much smaller than 1. Consequently, the approximation stated in (33) holds well within the context of such soft tissues.

Now, by applying the approximations (30) and (31) to (27), the Hessian operator simplifies to:

$$\begin{aligned} H^{(n)}(\mathbf{x}, \mathbf{x}') &= \sum_{e,r} \int \mathcal{Q}^{(n)}(\omega, r, e, \mathbf{x}) e^{-i\bar{\mathbf{k}}^{(n)}(\omega, r, e, \mathbf{x}') \cdot (\mathbf{x} - \mathbf{x}')} \mathcal{D}^{(n)}(\omega, r, e, \mathbf{x}', \mathbf{x}') d\omega \\ &= \iiint \frac{1}{\Delta e \Delta r} \mathcal{Q}^{(n)}(\omega, r, e, \mathbf{x}) e^{-i\bar{\mathbf{k}}^{(n)}(\omega, r, e, \mathbf{x}') \cdot (\mathbf{x} - \mathbf{x}')} \mathcal{D}^{(n)}(\omega, r, e, \mathbf{x}', \mathbf{x}') d\omega dr de. \end{aligned} \quad (34)$$

Assuming that rays do not exhibit caustics or other singularities, the integration variables are transformed using the one-to-one mapping $(\omega, r, e) \rightarrow (|\bar{\mathbf{k}}|, \zeta, \theta)$. The scattering angle $\theta(\omega, r, e, \mathbf{x}')$ at an arbitrary point \mathbf{x}' and emitter-receiver pair (e, r) is defined as:

$$\theta(\omega, r, e, \mathbf{x}') = [\gamma(\omega, \mathbf{x}', r) + \pi] - \gamma(\omega, \mathbf{x}', e), \quad (35)$$

where $\gamma(\omega, \mathbf{x}', e)$ (resp. $\gamma(\omega, \mathbf{x}', r)$) is the angle of the wavevector for a ray originating from e (resp. r). The additional π accounts for the phase reversal due to the scattered wave propagating from \mathbf{x}' to r . Figure 1 illustrates the ray parameterization at the scattering point \mathbf{x}' , with the dependence of parameters on ω omitted for simplicity.

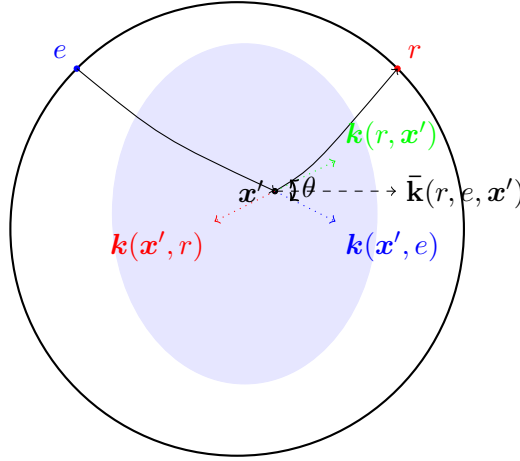


FIGURE 1. Ray parameterization at the scattering point \mathbf{x}' . The wavevectors $\mathbf{k}(\mathbf{x}', e)$ (blue) and $\mathbf{k}(\mathbf{x}', r)$ (red) correspond to rays emanating from the emitter e and receiver r , respectively, at \mathbf{x}' . These wavevectors are expressed in polar coordinates as $(k(\mathbf{x}'), \gamma(\mathbf{x}', e))$ and $(k(\mathbf{x}'), \gamma(\mathbf{x}', r))$. The vector $\bar{\mathbf{k}}(r, e, \mathbf{x}')$ passes through \mathbf{x}' and represents the gradient of a two-way isochron, computed as $\bar{\mathbf{k}}(r, e, \mathbf{x}') = \mathbf{k}(\mathbf{x}', e) + \mathbf{k}(r, \mathbf{x}')$. Its polar representation is given by $(|\bar{\mathbf{k}}(r, e, \mathbf{x}')|, \zeta(r, e, \mathbf{x}'))$. The phase-reversed wavevector $\mathbf{k}(r, \mathbf{x}')$ is represented in polar coordinates as $(k(\mathbf{x}'), \gamma(\mathbf{x}', r) + \pi)$. Additionally, $\theta(r, e, \mathbf{x}')$ denotes the scattering angle. The dependence on ω is omitted for brevity.

The pair $(|\bar{\mathbf{k}}|, \zeta)$ represents the polar coordinates of the two-way wavevector $\bar{\mathbf{k}}(\omega, r, e, \mathbf{x}')$, which is normal to the two-way isochron, associated with the accumulated phase $\phi(\omega, r, \mathbf{x}') + \phi(\omega, \mathbf{x}', e)$. Specifically:

$$|\bar{\mathbf{k}}| = 2k \cos\left(\frac{\theta}{2}\right), \quad (36)$$

$$\zeta(\omega, r, e, \mathbf{x}') = \frac{1}{2} \left[[\gamma(\omega, \mathbf{x}', r) + \pi] + \gamma(\omega, \mathbf{x}', e) \right]. \quad (37)$$

Applying the change of variables $(\omega, r, e) \rightarrow (|\bar{\mathbf{k}}|, \zeta, \theta)$ in (34), we obtain:

$$H^{(n)}(\mathbf{x}, \mathbf{x}') = \iiint \frac{1}{\Delta e \Delta r} \mathcal{Q}^{(n)}(\omega, r, e, \mathbf{x}) e^{-i\bar{\mathbf{k}}^{(n)}(\omega, r, e, \mathbf{x}') \cdot (\mathbf{x} - \mathbf{x}')} \times \mathcal{D}^{(n)}(\omega, r, e, \mathbf{x}', \mathbf{x}') \left| \frac{\partial(\omega, r, e)}{\partial(|\bar{\mathbf{k}}|, \zeta, \theta)} \right| d|\bar{\mathbf{k}}| d\zeta d\theta. \quad (38)$$

Here, \times indicates scalar multiplication. Following [26, 29, 30, 31], we choose $\mathcal{Q}^{(n)}$ to diagonalize $H^{(n)}(\mathbf{x}, \mathbf{x}')$, allowing inversion in a single step. Specifically, with:

$$\mathcal{Q}^{(n)}(\omega, r, e, \mathbf{x}) = \frac{\Delta e \Delta r}{(2\pi)^2} \frac{|\bar{\mathbf{k}}^{(n)}(\omega, r, e, \mathbf{x})|}{\mathcal{D}^{(n)}(\omega, r, e, \mathbf{x}, \mathbf{x})} \left| \frac{\partial(|\bar{\mathbf{k}}|, \zeta, \theta)}{\partial(\omega, r, e)} \right|, \quad (39)$$

the Hessian in (38) simplifies to:

$$H(\mathbf{x}, \mathbf{x}') = \int \left[\frac{1}{(2\pi)^2} \iint |\bar{\mathbf{k}}| e^{-i\bar{\mathbf{k}}(\mathbf{x}') \cdot (\mathbf{x} - \mathbf{x}')} d|\bar{\mathbf{k}}| d\zeta \right] d\theta \approx 2\pi \delta(\mathbf{x} - \mathbf{x}'). \quad (40)$$

The term in brackets in (40) represents a band-limited variant of the Fourier transform of the delta function in cylindrical coordinates, as given in [29]:

$$\frac{1}{(2\pi)^2} \int_{\zeta=0}^{2\pi} \int_{-\infty}^{+\infty} |\bar{\mathbf{k}}| e^{-i\bar{\mathbf{k}}(\mathbf{x}') \cdot (\mathbf{x} - \mathbf{x}')} d|\bar{\mathbf{k}}| d\zeta = \delta(\mathbf{x} - \mathbf{x}'). \quad (41)$$

The Jacobian determinant simplifies to:

$$\left| \frac{\partial(|\bar{\mathbf{k}}|, \zeta, \theta)}{\partial(\omega, r, e)} \right| = \left| \frac{\partial\gamma_e}{\partial e} \right| \left| \frac{\partial\gamma_r}{\partial r} \right| \left| \frac{\partial(|\bar{\mathbf{k}}|)}{\partial\omega} \right|, \quad (42)$$

where:

$$\frac{\partial(|\bar{\mathbf{k}}(\mathbf{x})|)}{\partial\omega} = 2 \cos\left(\frac{\theta(\mathbf{x})}{2}\right) \left[\frac{1}{c(\mathbf{x})} + y \tan\left(\frac{\pi y}{2}\right) \omega^{y-1} \alpha_0(\mathbf{x}) \right]. \quad (43)$$

3.4. The search direction formula. By substituting the weighting function in (39) into the functional gradient (25), and then inserting the result into the linearized equation (24) alongside (40), the search direction is derived as:

$$\delta m^{(n)}(\mathbf{x}') \approx \Re \left\{ \sum_{e,r,\omega} \Lambda^{(n)}(\omega, r, e, \mathbf{x}') g_{\text{res}}^{(n)}(\omega, r, e) \right\}. \quad (44)$$

Here, $\Re\{\cdot\}$ denotes the real part, and

$$\Lambda^{(n)}(\omega, r, e, \mathbf{x}') = \frac{\Delta e \Delta r \Delta\omega}{(2\pi)^3} \left| \frac{\partial\gamma^{(n)}(\omega, \mathbf{x}', e)}{\partial e} \right| \left| \frac{\partial\gamma^{(n)}(\omega, \mathbf{x}', r)}{\partial r} \right| \left| \frac{\partial(|\bar{\mathbf{k}}(\omega, r, e, \mathbf{x}')|)}{\partial\omega} \right| \times \quad (45)$$

$$|\bar{\mathbf{k}}^{(n)}(\omega, r, e, \mathbf{x}')| [\Upsilon_m^{(n)}(\omega, \mathbf{x}')]^{-1} g_{\dagger}^{(n)}(\omega, \mathbf{x}', e) g_{\dagger}^{(n)}(\omega, \mathbf{x}', r),$$

where

$$g_{\dagger}^{(n)}(\omega, \mathbf{x}, \mathbf{x}') = [A^{(n)}(\omega, \mathbf{x}, \mathbf{x}')]^{-1} \exp\left(-i[\phi^{(n)}(\omega, \mathbf{x}, \mathbf{x}') + \pi/4]\right). \quad (46)$$

The term g_{\dagger} is referred to as the *reversed* Green's function, where the dagger symbol (\dagger) signifies a reversal in both phase and amplitude. Specifically, for $g_{\dagger}^{(n)}(\omega, \mathbf{x}, r)$, which acts on $g_{\text{res}}^{(n)}(\omega, r, e)$, the reciprocity of the Green's function is utilized [40].

In Eq. (45), the parameters $|\partial\gamma(\omega, \mathbf{x}', e)/\partial e| \Delta e$ and $|\partial\gamma(\omega, \mathbf{x}', r)/\partial r| \Delta r$ are approximated using finite differences as follows:

$$\left| \frac{\partial\gamma(\omega, \mathbf{x}', e)}{\partial e} \right| \Delta e \approx \frac{1}{2} |\gamma(\omega, \mathbf{x}', e+1) - \gamma(\omega, \mathbf{x}', e-1)| \quad (47)$$

and

$$\left| \frac{\partial\gamma(\omega, \mathbf{x}', r)}{\partial r} \right| \Delta r \approx \frac{1}{2} |\gamma(\omega, \mathbf{x}', r+1) - \gamma(\omega, \mathbf{x}', r-1)|, \quad (48)$$

where $\gamma(\omega, \mathbf{x}', e \pm 1)$ (or $\gamma(\omega, \mathbf{x}', r \pm 1)$) denotes the adjacent emitters (or receivers).

The backprojection operator in Eq. (45) compensates for amplitude decay and phase shifts in the scattered waves by reversing both the incident and scattered Green's functions. The factors $|\partial\gamma(\omega, \mathbf{x}', e)/\partial e|\Delta e$ and $|\partial\gamma(\omega, \mathbf{x}', r)/\partial r|\Delta r$ account for the angular nonuniformity and sparsity with which emitters and receivers are observed by a scattering point \mathbf{x}' within the medium, respectively. The Born approximation, which inherently relies on a low-frequency assumption, considers that waves originating from emitter e and measured at receiver r may be scattered by any point in the medium. In contrast, the backprojection operator derived in Eq. (45) assumes that high-frequency components dominate the scattered waves. The correction factors $|\bar{\mathbf{k}}| |\partial(|\bar{\mathbf{k}}|)/\partial\omega$, incorporating the scattering angles θ , prioritize contributions from scatterers near the ray linking the emitter-receiver pair (e, r) over those further away. This high-frequency assumption aligns with the smoothness of the wavenumber map $k^{(n)}$, as utilized in the approximations (30) and (31), which hold more accurately at high frequencies.

Finally, the squared slowness is updated via $m^{(n+1)} = m^{(n)} + \tau \delta m^{(n)}$, where τ is the step length, fixed for all n . The updated sound speed $c^{(n+1)}$ is then computed from $m^{(n+1)}$.

4. RAY TRACING

This section details the numerical implementation of ray-based ultrasound tomography (UST) for heterogeneous and absorbing media. Specifically, it describes how ray theory, derived from high-frequency approximations and governed by the *Eikonal* equation (10) and *Transport* equation (11), is used to compute the approximate Green's function and its reversed counterpart.

4.1. Hamiltonian formulation of the Eikonal equation. The Eikonal equation can be expressed as a Hamiltonian system [41]:

$$H(\mathbf{x}, \mathbf{k}) = \frac{1}{2}k^{-1}[\mathbf{k} \cdot \mathbf{k} - k^2], \quad (49)$$

where k , the real part of \tilde{k} , is dependent on the sound speed c via Eq. (3). Along a ray, $H = 0$, and the system satisfies the canonical equations:

$$\begin{aligned} \dot{\mathbf{x}} &= \nabla_{\mathbf{k}} H, \\ \dot{\mathbf{k}} &= -\nabla_{\mathbf{x}} H. \end{aligned} \quad (50)$$

Correspondingly, the ray's position \mathbf{x} and wavevector \mathbf{k} satisfy:

$$\dot{\mathbf{x}} = k^{-1}\mathbf{k}, \quad \dot{\mathbf{k}} = \frac{1}{2}\nabla k[k^{-2}\mathbf{k} \cdot \mathbf{k} + 1], \quad (51)$$

where $k^{-2}|\mathbf{k}|^2 = 1$ for $H = 0$.

For each emitter-receiver pair (e, r) , the ray is described by the canonical vector $\mathbf{y}(s) = [\mathbf{x}(s), \mathbf{k}(s)]^T$, where s denotes the arc length. The ray's initial position \mathbf{x}_0 coincides with the emitter position e on the ring, while the initial wavevector $\mathbf{k}(s_0)$ is determined through *ray linking* [36], ensuring the ray intersects the receiver position r . Further details on ray linking are provided later in this section.

4.2. Ray Jacobian and paraxial equations. The amplitude factor A in Eq. (9) includes contributions from geometrical spreading, denoted A_{geom} , determined by the *Transport* equation (11). This equation describes changes in the ray tube area relative to a reference ray, relying on the *ray Jacobian* [27]. Previously, the ray Jacobian was computed using finite differences of auxiliary rays near the reference ray [1, 42]. Here, *paraxial ray tracing*, also known as *dynamic ray tracing*, is employed instead.

Paraxial ray tracing involves solving an additional system of linear ordinary differential equations alongside the reference ray, eliminating the need for independent auxiliary rays. For each emitter-receiver pair, the paraxial ray perturbation vector $\delta\mathbf{y}(s) = [\delta\mathbf{x}(s), \delta\mathbf{k}(s)]^T$ satisfies the system:

$$\delta\dot{\mathbf{y}} = \mathbf{D} \delta\mathbf{y}, \quad (52)$$

where

$$\mathbf{D} = \begin{bmatrix} \nabla_{\mathbf{x}} \nabla_{\mathbf{k}} H & \nabla_{\mathbf{k}} \nabla_{\mathbf{k}} H \\ -\nabla_{\mathbf{x}} \nabla_{\mathbf{x}} H & -\nabla_{\mathbf{k}} \nabla_{\mathbf{x}} H \end{bmatrix}. \quad (53)$$

The paraxial ray perturbation equations are:

$$\begin{aligned} \delta\dot{\mathbf{x}} &= \left[\frac{\partial \dot{\mathbf{x}}}{\partial \mathbf{x}} \right] \delta\mathbf{x} + \left[\frac{\partial \dot{\mathbf{x}}}{\partial \mathbf{k}} \right] \delta\mathbf{k}, \\ \delta\dot{\mathbf{k}} &= \left[\frac{\partial \dot{\mathbf{k}}}{\partial \mathbf{x}} \right] \delta\mathbf{x} + \left[\frac{\partial \dot{\mathbf{k}}}{\partial \mathbf{k}} \right] \delta\mathbf{k}, \end{aligned} \quad (54)$$

where

$$\begin{aligned} \frac{\partial \dot{\mathbf{x}}}{\partial \mathbf{x}} &= -k^{-2} \mathbf{k} \nabla_{\mathbf{k}}^T, & \frac{\partial \dot{\mathbf{x}}}{\partial \mathbf{k}} &= k^{-1}, \\ \frac{\partial \dot{\mathbf{k}}}{\partial \mathbf{x}} &= \nabla^2 k - k^{-1} \nabla k \nabla_{\mathbf{k}}^T, & \frac{\partial \dot{\mathbf{k}}}{\partial \mathbf{k}} &= k^{-2} \nabla k \mathbf{k}^T. \end{aligned} \quad (55)$$

4.3. Numerical implementation. Here, the paraxial ray tracing system defined by (51) and (54) is numerically implemented using Heun's method, a second-order variant of the Runge-Kutta (RK) scheme that balances computational efficiency and accuracy [43, 44]. An outline of Heun's approach for solving the paraxial ray tracing equations is provided in Algorithm 1. In this implementation, normalization steps are applied to the wavevector \mathbf{k} as a safeguard to enhance the stability of the algorithm in cases where wavenumber maps exhibit sharp gradients. However, numerical experiments show that for soft tissues, such as breast tissue, where refractive index variations are within the range of 0.9 to 1.1, the normalization steps have negligible effects on ray trajectories and can thus be omitted if desired. The system (52) represents a ray if the perturbation vector $\delta\mathbf{y}$ satisfies

$$\delta H = \nabla_{\mathbf{k}} H \cdot \delta\mathbf{k} + \nabla_{\mathbf{x}} H \cdot \delta\mathbf{x} = 0. \quad (56)$$

Additionally, as per (51), δH remains constant along any solution of the paraxial system. Consequently, it is sufficient to ensure the condition (56) is met at the initial point [41].

4.4. Initial conditions for ray tracing. The initial wavevector is determined by the frequency ω , the sound speed in water c_0 , and the initial unit direction vector. Following [1], the rays are initialized at the emitter position e and connected to the receiver position r using ray linking [36]. Ray linking, a type of shooting method, identifies a ray trajectory that provides a stationary path within a family of neighboring paths between e and r . This is achieved by imposing a boundary condition on the ray's path such that the ray initialized at the emitter position e intersects the receiver position r after traversing the medium. For each linear subproblem in the UST inverse problem, ray linking is performed for each emitter-receiver pair (e, r) . This involves iteratively adjusting the initial unit direction of the ray originating at e using an optimization algorithm to ensure that the ray intercepts the detection surface (ring) at the receiver position r within a specified tolerance [27, 36].

Once the initial wavevector $\mathbf{k}(s_0)$ is determined, the condition (56), along with the enforcement of $\delta\mathbf{x}(s_0) = 0$, requires the initial perturbation $\delta\mathbf{k}(s_0)$ to satisfy

$$\mathbf{k}(s_0) \cdot \delta\mathbf{k}(s_0) = 0. \quad (57)$$

Algorithm 1 Paraxial ray tracing for the linked ray initialized on e and intercepted by r using Heun’s method

```

1: input:  $(e, r)$ ,  $k := k(\mathbf{x})$            ▷ Input emitter and receiver positions and wavenumber map
2: initialize:  $\mathbf{x} = e$ ,  $\mathbf{k}$            ▷ Set initial position, and compute the initial wavevector through ray
   linking
3:  $\delta\mathbf{x} = 0$ ,  $\delta\mathbf{k}$  satisfying  $\delta\mathbf{k} \cdot \mathbf{k} = 0$ ,           ▷ Set initial conditions: paraxial ray (amplitude)
4: while  $\mathbf{x}(s)$  is inside  $\Omega$  do
5:
6:   – – –                               ▷ Update reference ray
7:    $\mathbf{k} \leftarrow k \mathbf{k} / |\mathbf{k}|$                                ▷ Normalize the ray direction
8:    $q_x = \mathbf{k}/k$                                            ▷ Compute the update variables
9:    $q_k = \nabla k(\mathbf{x})$ 
10:   $\mathbf{k}' \leftarrow \mathbf{k} + \Delta s q_k$                                ▷ Update the auxiliary ray direction
11:   $k' \leftarrow k(\mathbf{x} + \Delta s q_x)$                                ▷ Update the auxiliary wavenumber
12:   $\mathbf{k}' \leftarrow k' \mathbf{k}' / |\mathbf{k}'|$                                ▷ Normalize the auxiliary ray direction
13:   $q'_x = \mathbf{k}'/k'$                                            ▷ Compute the auxiliary update variables
14:   $q'_k = \nabla k(\mathbf{x} + \Delta s q_x)$ 
15:   $\mathbf{x} \leftarrow \mathbf{x} + \Delta s [q_x + q'_x] / |q_x + q'_x|$            ▷ Update the ray position
16:   $\mathbf{k} \leftarrow \mathbf{k} + \Delta s [q_k + q'_k] / 2$            ▷ Update the ray direction
17:
18:   – – –                               ▷ Update paraxial ray: geometrical amplitude
19:    $q_{\delta\mathbf{x}} = [-\mathbf{k} \nabla k^T / k^2] \delta\mathbf{x} + [1/k] \delta\mathbf{k}$            ▷ Compute the update variables
20:    $q_{\delta\mathbf{k}} = [\nabla^2 k - \nabla k \nabla k^T / k] \delta\mathbf{x} + [\nabla k \mathbf{k}^T / k^2] \delta\mathbf{k}$ 
21:    $\delta\mathbf{k}' \leftarrow \delta\mathbf{k} + \Delta s q_{\delta\mathbf{k}}$                                ▷ Update the auxiliary ray direction perturbation
22:    $\delta\mathbf{x}' \leftarrow \delta\mathbf{x} + \Delta s q_{\delta\mathbf{x}}$                                ▷ Update the auxiliary ray position perturbation
23:    $q'_{\delta\mathbf{x}} = [-\mathbf{k}' \nabla k'^T / k'^2] \delta\mathbf{x}' + [1/k'] \delta\mathbf{k}'$            ▷ Compute the auxiliary update variables
24:    $q'_{\delta\mathbf{k}} = [\nabla^2 k' - \nabla k' \nabla k'^T / k'] \delta\mathbf{x}' + [\nabla k' \mathbf{k}'^T / k'^2] \delta\mathbf{k}'$ 
25:    $\delta\mathbf{x} \leftarrow \delta\mathbf{x} + \Delta s [q_{\delta\mathbf{x}} + q'_{\delta\mathbf{x}}] / 2$            ▷ Update the ray position perturbation
26:    $\delta\mathbf{k} \leftarrow \delta\mathbf{k} + \Delta s [q_{\delta\mathbf{k}} + q'_{\delta\mathbf{k}}] / 2$            ▷ Update the ray direction perturbation
27:
28: end while

```

4.5. Interpolation. *Grid-to-ray interpolation:* The squared slowness map is defined on grid points. To implement Algorithm 1, this map must be interpolated onto the sampled points along the rays. In this study, grid-to-ray interpolation is performed using B-spline interpolation, which provides smooth and continuous values for both ∇k and $\nabla^2 k$ at any arbitrary (off-grid) point. For further details, refer to [1].

Ray-to-grid interpolation: The parameters of the Green’s function at grid points are computed by interpolating data from the linked rays back onto the grid. This is achieved using trilinear interpolation, as detailed in [1].

5. RAY COORDINATES

This section describes how the Green’s function in the residual (19) and its reversed variants in the backprojection operator (45) are approximated and discretized along linked rays to compute the update direction (44) for each linearized frequency subproblem. The derivations will focus on $g(\omega, r, e)$ and $g_\dagger(\omega, \mathbf{x}, e)$; however, the formulae for $g_\dagger(\omega, \mathbf{x}, e)$ can be similarly applied to $g_\dagger(\omega, \mathbf{x}, r)$

by interchanging e and r . In general, for the 2D case, rays are parameterized using two coordinates: one specifying the initial direction (angle) of the ray and another representing a monotonic parameter along the ray [27]. Here, the ray parameters are chosen as the initial angle, β , and the arc length, s .

Definition 1. The trajectory of a ray linking an emission point e to a reception point r is defined by the sampled arc lengths s_i , where $i \in \{0, \dots, M_{(e,r)}\}$. The sampled points start at s_0 , with $\mathbf{x}(s_0) := e$, and end at $s_{M_{(e,r)}}$, with $\mathbf{x}(s_{M_{(e,r)}}) := r$, the position of receiver r . The sampled arc lengths s_i are defined as:

$$s_i = \begin{cases} i\Delta s, & \text{for } i \in \{0, \dots, M_{(e,r)} - 1\}, \\ (i-1)\Delta s + \Delta s', & \text{for } i = M_{(e,r)}, \end{cases} \quad (58)$$

where the second case ensures that the last point of the ray coincides with the reception point r , and $\Delta s' = s_{M_{(e,r)}} - s_{M_{(e,r)}-1}$ satisfies $\Delta s' \leq \Delta s$ [36].

Definition 2. For each emitter position e , the Green's function parameters are approximated along a set of linked rays defined by $f_{(k,r,e)} = 0$. These rays are parameterized in space as $\mathbf{x}(s_i, \beta_{(r,e)})$, denoting the position at arc length s_i along a ray linking emitter position e to receiver position r , with the ray's polar initial direction given by $\beta_{(r,e)}$.

Using the coordinates defined in Definition 2, the Green's function $g(\omega, \mathbf{x}, e)$ and its reversed variant $g_{\dagger}(\omega, \mathbf{x}, e)$ are discretized at points sampled along the rays linking emitter e to all receivers r as:

$$g(\omega, \mathbf{x}(s_i, \beta_{(r,e)}), e) \approx A(\omega, \mathbf{x}(s_i, \beta_{(r,e)}), e) \exp\left(i[\phi(\omega, \mathbf{x}(s_i, \beta_{(r,e)}), e) + \pi/4]\right), \quad (59)$$

and

$$g_{\dagger}(\omega, \mathbf{x}(s_i, \beta_{(r,e)}), e) \approx [A(\omega, \mathbf{x}(s_i, \beta_{(r,e)}), e)]^{-1} \exp\left(-i[\phi(\omega, \mathbf{x}(s_i, \beta_{(r,e)}), e) + \pi/4]\right), \quad (60)$$

where $e := \mathbf{x}(s_0, \beta_{(r,e)})$ for all r (cf. (9) and (46)).

In (59) and (60), the accumulated phase ϕ is discretized as:

$$\phi(\omega, \mathbf{x}(s_i, \beta_{(r,e)}), e) = \int_{s_0}^{s_i} k(\mathbf{x}(s, \beta_{(r,e)})) ds - \frac{\pi}{2} \mathcal{K}(s_i, \beta_{(r,e)}), \quad (61)$$

where $\mathcal{K}(s_i, \beta_{(r,e)})$ is the cumulative count of caustics (points where the ray Jacobian changes sign), each contributing a $\pi/2$ phase shift [27].

The amplitude factor A has contributions from absorption, A_{abs} , discretized as:

$$A_{\text{abs}}(\omega, \mathbf{x}(s_i, \beta_{(r,e)}), e) = \exp\left(-\int_{s_0}^{s_i} \alpha(\mathbf{x}(s, \beta_{(r,e)})) ds\right), \quad (62)$$

and from geometrical spreading, A_{geom} , given by:

$$A_{\text{geom}}(\omega, \mathbf{x}(s_i, \beta_{(r,e)}), e) = \left[\frac{c(\mathbf{x}(s_i, \beta_{(r,e)})) J(s_1, \beta_{(r,e)})}{c(\mathbf{x}(s_1, \beta_{(r,e)})) J(s_i, \beta_{(r,e)})} \right]^{1/2} A_{\text{geom}}(\omega, \mathbf{x}(s_1, \beta_{(r,e)}), e), \quad (63)$$

where $J(s_i, \beta_{(r,e)}) = \det \Xi(s_i, \beta_{(r,e)})$ is the ray's Jacobian, and $\Xi = \partial \mathbf{x} / \partial \eta$ is the transformation matrix from ray coordinates $\eta = [\eta_1, \eta_2]^T$ (with $\eta_1 = \beta$ and $\eta_2 = s$) to Cartesian coordinates $\mathbf{x} = [\mathbf{x}_1, \mathbf{x}_2]^T$ [27]. Additionally, s_1 is the arc length of the first sampled point after the initial point on the ray. This point is chosen as the reference point, on which the amplitude is calculated analytically.

6. NUMERICAL RESULTS

This section describes numerical experiments demonstrating the effectiveness of the proposed ray-based inversion approach for low-cost computation of a high-resolution image of the sound speed distribution inside the breast.

6.1. Data simulation. An imaging system consisting of 64 emitters and 256 receivers uniformly distributed along a circular ring with a radius of $R = 9.5$ cm was simulated. A horizontal slice of a 3D digital phantom, freely available from [45], was used to mimic the acoustic properties of the breast. The sound speed was set within the range of 1470–1580 m/s, the absorption coefficient α_0 within 0–1 dB MHz^{-y} cm⁻¹, and the power-law exponent y was fixed at 1.4. Figures 2(a) and 2(b) depict the sound speed and absorption coefficient maps of the breast phantom, respectively. For water, the sound speed and absorption coefficient were set to 1500 m/s and 0, respectively.

The computational domain comprised a grid of 502×502 points covering the region $[-10.04, +10.00] \times [-10.04, +10.00]$ cm², with a uniform grid spacing of $\Delta x = 0.4$ mm. Based on this sound speed distribution and grid spacing, the maximum frequency supported by the grid, f_{\max} , was determined to be 1.84 MHz.

Simulating time series data. A *k*-space pseudo-spectral method was employed to simulate the acoustic pressure time series data on the detection ring, generated by each time-varying source s . This numerical approach, implemented in an open-source toolbox [35], solves a system of three coupled first-order wave equations equivalent to Szabo’s second-order wave equation.¹ Szabo’s wave equation is a time-domain variant of Eq. (2), with the complex wavenumber defined by Eq. (3) [32, 33, 34, 35].

The emitters and receivers were modeled as point transducers distributed along the circular detection ring. The interpolation of the pressure field between the computational grid and these transducers was performed using a Fourier interpolation approach [35]. Each emitter was individually driven by an excitation pulse, and the resulting acoustic pressure time series were recorded on the receivers at 6466 time points with a sampling rate of 39.6 MHz (25.25 ns time spacing). This procedure was repeated for all emitters.

Figure 3(a) presents the normalized amplitude of the acoustic source in the time domain, while Figure 3(b) illustrates the normalized amplitude and phase components of the acoustic source in the frequency domain. This signal was consistently used as the acoustic source for all excitations.

6.2. Numerical validation of the ray approximation to the Green’s function. This section compares the approximate Green’s function solution to Szabo’s wave equation with a full-wave solution computed using the *k*-space pseudo-spectral method [33, 34, 35] in a heterogeneous and absorbing medium with spatially smooth variations in acoustic properties. The approximate heterogeneous Green’s function was introduced in Section 2, and its numerical approximation and discretization were described in Sections 4 and 5, respectively. Further details about the derivation of the Green’s function solution to Szabo’s wave equation were provided in [1].

For the full-wave simulation, emitter 1 was excited by the acoustic pulse shown in Figures 3(a), and the induced pressure propagated through the breast immersed in water and was recorded on all 256 receivers. The Green’s function, $g(\omega, r, e)$, depends on the accumulated parameters and geometrical spreading along the linked rays, but does not account for scattering effects. Therefore, to enable

¹In this study, the k-Wave toolbox [35] was modified to accommodate the inclusion of point sources in terms of s , as these sources were assumed in the modeling process. This modification was necessary to align with the specific assumptions of the study and was carried out in accordance with the guidelines outlined in Section 6.1 of [49]. This approach ensures that the simulation settings were consistent with best practices for modeling point sources, and the modification has been consistently documented throughout the manuscript.

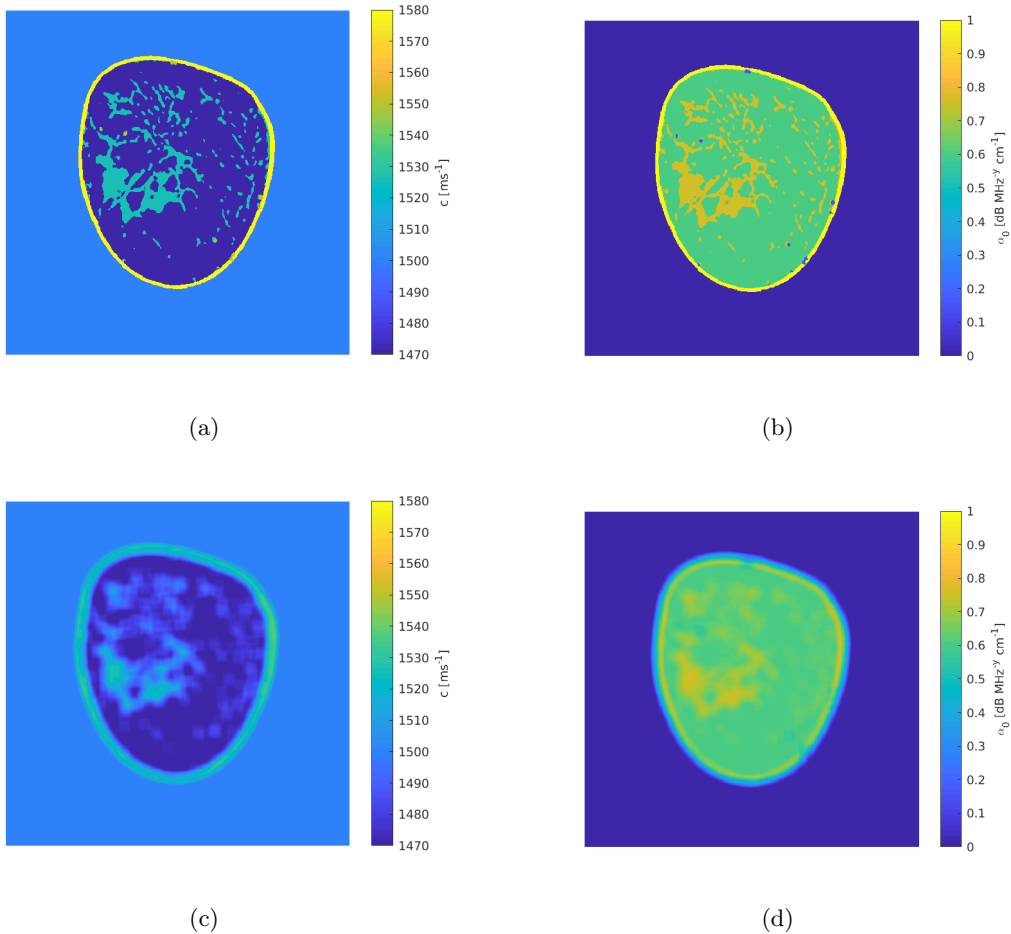


FIGURE 2. Phantom used for simulation of synthetic UST data using the full-wave approach: (a) sound speed [ms^{-1}], (b) absorption coefficient [$\text{dB MHz}^{-y} \text{cm}^{-1}$], (c) smoothed sound speed [ms^{-1}], (d) smoothed absorption coefficient [$\text{dB MHz}^{-y} \text{cm}^{-1}$]. The maps are shown on a grid consisting of 502×502 points (used for the wave simulation). The maps in (c) and (d) are smoothed by applying an averaging window of size 17 points to the original acoustic maps in (a) and (b), respectively. The original (nonsmoothed) acoustic maps were used for simulating the data for image reconstruction, and the smoothed maps were used for simulating the data for benchmarking against the ray approximation to the heterogeneous Green's function. The power law exponent was assumed to be $y = 1.4$ and homogeneous.

a fair comparison with the full-wave simulation, scattering effects were minimized by applying an averaging window of 17 grid points to the sound speed and absorption coefficient maps. The smoothed maps are shown in Figures 2(c) and 2(d), respectively.

For the ray approximation, the Green's function was computed along the linked rays and then incorporated into the Green's formula, Eq. (7), to approximate the pressure time series on the receivers after exciting emitter 1. Note that the spatial integral in Eq. (7) is omitted for a point source.

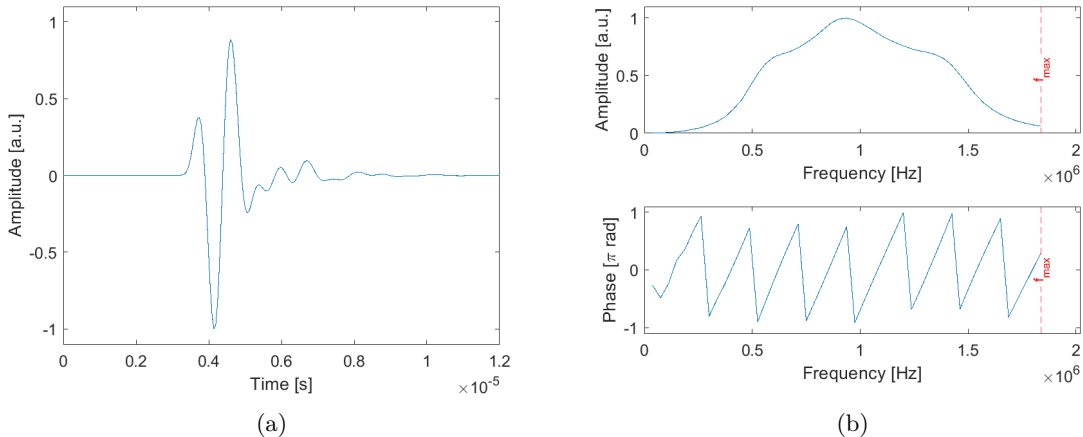


FIGURE 3. Acoustic source used for all excitations (emitters): (a) time domain, (b) frequency domain: normalized amplitude and phase. f_{\max} indicates the maximum frequency supported by the grid used for the wave simulations.

To avoid the inverse crime in the image reconstruction process, two different computational grids were used for data simulation and reconstruction. (This distinction may not be strictly necessary in this study, as inherently different approaches are used for simulation and reconstruction.) For ray-based image reconstruction, the computational grid had 204×204 points with a grid spacing of 1 mm. The ray approximation to the Green’s function used for comparison was also performed on this grid.

To implement the ray approximation, the smoothed sound speed and absorption coefficient maps from the full-wave simulation were interpolated onto the reconstruction grid. The interpolated wavenumber map was further smoothed using an averaging window of 7 grid points to minimize interpolation effects. (This window size was scaled inversely with the grid spacing increase compared to the full-wave grid.) The pressure field generated by emitter 1 was approximated on all 256 receivers at a single frequency of 1 MHz for three cases: (1) only water, (2) a non-absorbing breast immersed in water, and (3) an absorbing breast immersed in water.

Figure 4(a) shows the phase of the pressure time series on all receivers after emitter 1’s excitation. (Phases were wrapped to $[-\pi, \pi]$.) The green plot represents phases analytically computed using the homogeneous Green’s function assuming only water, while the red plot shows phases computed using the ray approximation for the absorbing breast. The blue plot represents the phases from the full-wave simulation for the absorbing breast. For receivers in the range of 50–180, where rays traverse the breast, the ray approximation and full-wave simulation show strong agreement. In contrast, the homogeneous Green’s function yields large discrepancies.

Figure 4(b) illustrates the amplitude of the pressure time series on all receivers after emitter 1’s excitation. The green plot shows amplitudes computed using the homogeneous Green’s function (only water). Amplitudes assuming a non-absorbing breast, attenuated solely by geometrical spreading, were computed via Eq. (63) and are shown in light blue. (For Eq. (63), the Jacobian was approximated using paraxial ray tracing, as detailed in Section 4.) The red plot represents amplitudes computed for the absorbing breast, incorporating attenuation due to geometrical spreading (light blue) and accumulated absorption using Eq. (62). The dark blue plot shows amplitudes from the full-wave simulation. For the absorbing breast, the ray approximation combining geometrical

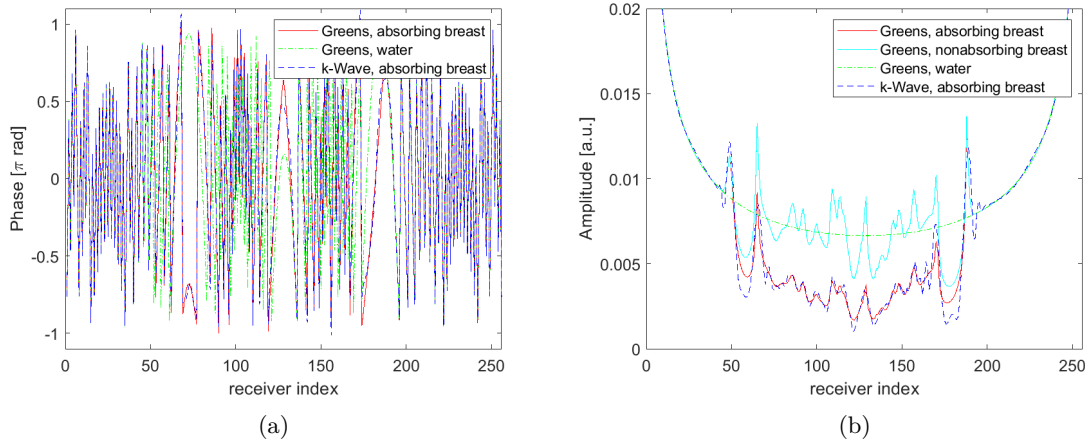


FIGURE 4. The pressure time series on all 256 receivers at a single frequency of 1 MHz after an excitation of emitter 1: (a) phase, (b) amplitude. (For the k-Wave simulation, because point sources in terms of s are used, the inclusion of the source follows Section 6.1 in [49].)

spreading and accumulated absorption closely agrees with the full-wave results, while the homogeneous Green’s function or the heterogeneous Green’s function neglecting absorption show significant discrepancies.

6.3. Image reconstruction. This subsection outlines the ray-based image reconstruction process from ultrasound data simulated using the full-waveform approach and presents the reconstructed images. Synthetic data were simulated using the k -space pseudo-spectral approach, as described in Section 6.1. Two datasets were generated: the first simulated in water alone, and the second simulated using the digital breast phantom immersed in water. The breast-in-water data employed the sound speed and absorption coefficient maps shown in Figures 2(a) and 2(b), respectively. For each dataset, emitters were sequentially excited by the pulse shown in Figure 3(a), and the resulting pressure time series were recorded on all receivers. This process was repeated for all emitters.

The simulation of the UST dataset for the digital breast phantom immersed in water, using the k-Wave MATLAB toolbox [35] on a single 6-core Intel Xeon E5-2620 v2 2.1 GHz CPU, required approximately 4 hours. Additive white Gaussian noise (AWGN) was introduced to the simulated time series at varying levels to achieve signal-to-noise ratios (SNRs) of 40 dB, 30 dB, and 25 dB based on the peak amplitudes, for both datasets.

To mitigate the inverse crime related to temporal discretization, the time series simulated by the full-waveform approach were downsampled by a factor of 2 before ray-based reconstruction. The reconstruction grid consisted of 204×204 points, spanning the region $[-10.1650, +10.1350] \times [-10.1650, +10.1350]$ cm², with a uniform grid spacing of $\Delta x = 1$ mm. Image reconstruction was confined to grid points inside a binary mask with a radius equal to 90% of the detection ring’s radius, while sound speed values outside this mask were set to that of water (1500 ms⁻¹).

The Green’s function g , utilized in the residual g_{res} , was approximated directly at the receiver locations through ray linking. Since the sound speed reconstruction is performed at grid points, the parameters of the reversed Green’s functions, g_{\uparrow} , defined along the linked rays, were interpolated

onto the grid points. This interpolation involved applying triangulation to the sampled points along the linked rays and using trilinear interpolation.

Furthermore, the reversed Green's functions, $g_{\dagger}(\omega, \mathbf{x}, r)$, were computed without additional ray tracing by reversing the accumulated parameters of the forward Green's functions, $g(\omega, r, e)$ [1]. To calculate the geometrical components of the amplitudes for $g_{\dagger}(\omega, \mathbf{x}, r)$, a paraxial ray was traced along each reversed ray. Finally, the reversed (reciprocal) Green's functions, g_{\dagger} , were derived from the Green's functions, g , by reciprocating their phases and amplitudes.

6.3.1. Inversion approach using Time-of-Flights (initial guess). To address the high nonlinearity of the objective function in Eq. (18), an initial guess is often employed [10, 11]. In this work, an image reconstruction approach based on direct time-of-flights (TOFs) derived from the measured (simulated) pressure time series was utilized to provide an initial guess. The TOF-based inversion approach iteratively minimizes the L2 norm of the discrepancy between TOFs modeled via a ray tracing algorithm and TOFs extracted from the measured (simulated) pressure time series using a first-arrival picking algorithm [8].

To mitigate the effects of measurement errors on the picked first-arrivals, a difference inversion approach was employed. In this method, the difference in slowness ($1/c$) between the breast-in-water and only-water cases is computed from the discrepancy in first-arrival times obtained from the respective data sets. The minimization procedure iteratively linearizes the associated objective function and solves the resulting linear subproblems using a Radon-type technique.

Each linearized subproblem was solved using the Simultaneous Algebraic Reconstruction Technique (SART), which accounts for the nonuniform ray density resulting from the curved trajectories of the rays [46]. In each linearization step, the sound speed update was smoothed using an averaging window of 7 grid points, specifically for the purpose of ray tracing. However, the integration of accumulated TOFs along the ray trajectories was performed using the nonsmoothed sound speed updates. In practice, this meant that the system matrix was constructed based on the smoothed sound speed update, but the matrix was multiplied by the nonsmoothed update to retain accuracy. Ray linking was carried out using the Secant method. For each linearization, the linked ray (the optimal ray obtained after ray linking) for each emitter-receiver pair served as the initial guess for ray linking in the subsequent linearized subproblem for the same emitter-receiver pair [1, 36]. The TOF-based algorithm was terminated after a limited number of linearizations to achieve a balance between reconstruction accuracy and artifacts caused by errors in the picked first-arrival times [1].

6.3.2. Inversion approaches using ray approximation to heterogeneous Green's function. Below, the procedure for implementing the inversion approach based on the Green's function is explained. To evaluate the effectiveness of the proposed Hessian-free inversion approach, the method used in [1] serves as the benchmark. The goal of the inversion is to determine the squared slowness map, m , which minimizes the objective function (18). This problem is solved by discretizing the objective function at a range of frequencies within the frequency band of the transducers, and performing linearization and minimization from low to high frequencies until the computed update direction for the linearized subproblem associated with a frequency set becomes smaller than a specified tolerance. To compute the residual (19), the measured Green's function $\hat{g}(\omega, r, e)$ is derived by deconvolving the excitation pulse from the measured (simulated) pressure time series. Additionally, each Green's function $g(m; \omega, r, e)$ included in the residual (19) is approximated at the last points of the linked rays, computed using the most recent update of the sound speed.

Ray linking. For the TOF-based and the Green's function-based approaches, the ray linking was performed on the updates of the sound speed and wavenumber maps for each of emitter-receiver pairs separately. For each update of the wavenumber map and each emitter-receiver pair, the

ray linking was done by iteratively updating the initial unit direction of the ray using a Secant method [1, 36]. The initial guess for the unknown initial unit direction of the ray was set the obtained optimal initial direction after ray linking for the last previous update of the wavenumber map, and the ray’s trajectory was iteratively computed using the first part of Algorithm 1 until the interception point of the ray by the detection ring matches the receiver position within a tolerance. The parameters of Green’s functions g and reversed Green’s functions g_{\dagger} (included in the backprojection formula for the Hessian-free approach) were computed along the linked rays. (See the formulae given in section 5.) For computing the geometrical portion of amplitudes, linked rays are used as reference rays, and paraxial rays are computed in vicinity of the reference rays via implementing the second part of Algorithm 1. For ray tracing and ray linking, an averaging window of size 7 grid points was applied on the updated wavenumber maps, but integration along the linked rays and approximating the Green’s functions using the formulae in section 5 were applied on the nonsmoothed updates.

a) Hessian-free ray-Born inversion. The inversion approach described in section 3 was implemented using 140 discretized frequencies in the range $f \in \{0.2, \dots, 1.5\}$ MHz. Image reconstruction progressed sequentially from low to high frequencies, with each update of the squared slowness map computed at two consecutive frequencies using Eq. 44 ($n \in \{1, \dots, 70\}$). For each linearization step n , the Green’s functions $g(\omega, r, e)$ included in the residual (19), and the reversed Green’s functions $g_{\dagger}(\omega, \mathbf{x}, e)$ and $g_{\dagger}(\omega, \mathbf{x}, r)$ included in the backprojection formula (45), were computed along the forward and backward rays, respectively. The step length was heuristically chosen as $\tau = 1.2 \times 10^{-1}$ for all linearization steps.

The dominant computational cost in solving each linearized subproblem (24) arose from ray tracing, as the update direction was computed in a single step using Eq. 44. Consequently, the computational cost of solving each linearized subproblem using this method was comparable to that of the TOF-based algorithm. However, the total number of linearization steps required to reach an optimal solution with this approach was approximately five to ten times greater than that of the TOF-based algorithm.

b) Hessian-based ray-Born inversion (Gauss-Newton). This approach employs a specific weighting, with $\mathcal{Q} = 1$ for all $(\omega, r, e, \mathbf{x})$. Each linearized subproblem n (24) is solved by first forming the gradient $\nabla \mathcal{F}^{(n)}$ and then determining the update direction through iterative computations of the actions of the Hessian matrix $H^{(n)}$ on perturbations to the squared slowness map. This iterative procedure, using inner iterations, effectively produces a Gauss-Newton search direction. Each linearized subproblem in this study was solved using 10–15 inner iterations, with early termination of these iterations providing a regularizing effect on the solution. Details of the algorithm can be found in [1].

To benchmark the proposed Hessian-free ray-Born inversion algorithm, the Hessian-based inversion approach outlined in [1] was implemented at 100 discretized frequencies in the range $f \in \{0.2, \dots, 1.1\}$ MHz. Similar to the Hessian-free approach, the image reconstruction proceeded from low to high frequencies, with each update of the sound speed computed at two consecutive discretized frequencies ($n \in \{1, \dots, 50\}$). Compared to the Hessian-free approach, the Hessian-based algorithm required fewer linearisation steps, as solving subproblems at frequencies beyond 1.1 MHz resulted in negligible search directions. The step length was heuristically set to $\tau = 2.75 \times 10^4$ for all linearisations. Using the developed MATLAB code on the CPU described in the first paragraph of section 6.3, the computational time for solving each linearized subproblem n and computing the update direction was approximately an order of magnitude higher than the corresponding computational cost for the proposed Hessian-free approach.

As described in section 4, the geometrical amplitudes were computed by solving a paraxial system of equations rather than using auxiliary rays, as previously done in [1, 42] (see Algorithm 1).

The total computational time for reconstructing a sound speed image using the Hessian-based algorithm was approximately equivalent to the time required to simulate the breast-in-water and only-water UST datasets using k-Wave—essentially comparable to solving a single iteration of the full-waveform inversion approach [35]. As described in Section 3, updates to the sound speed map, c , were derived from the updates to the squared slowness map, m .

6.4. Reconstructed images. This section presents the sound speed images reconstructed using the proposed Hessian-free ray-Born inversion approach and compares them with images reconstructed using the Hessian-based inversion approach described in [1]. As noted earlier, the proposed Hessian-free approach is approximately an order of magnitude faster than the Hessian-based method.

The reconstructed images are evaluated using the Relative Error (RE), defined as:

$$RE_{\text{image}} = \frac{\|c_{\text{image}} - c_{\text{phantom}}\|_2}{\|c_{\text{water}} - c_{\text{phantom}}\|_2} \times 100, \quad (64)$$

where c_{phantom} represents the sound speed map of the digital breast phantom interpolated onto the reconstruction grid, and c_{image} is the reconstructed sound speed image. These quantities were calculated only on grid points within the binary mask used for image reconstruction. For grid points outside this mask, the sound speed was set to $c_{\text{water}} = 1500 \text{ ms}^{-1}$. (cf. Section 6.3). Reconstructed sound speed images are presented for synthetic datasets with signal-to-noise ratios (SNRs) of 40 dB, 30 dB, and 25 dB.

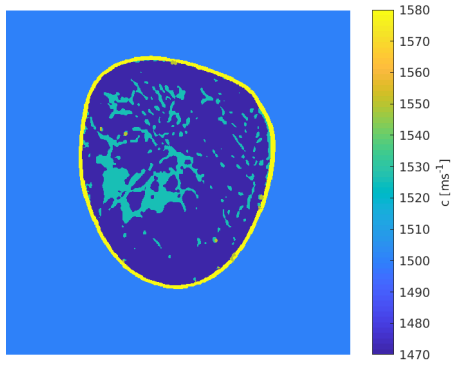
6.4.1. Reconstructed images from UST data with high SNR. This subsection focuses on the reconstructed sound speed images from synthetic ultrasound tomography (UST) data with an SNR of 40 dB, along with their evaluation in terms of RE. Figure 5(a) displays the sound speed map of the digital breast phantom (ground truth), while Figure 5(b) shows the image reconstructed from time-of-flights (TOFs) extracted using a modified Akaike Information Criterion (AIC) approach [8].

As discussed in Section 2, the proposed forward model, which uses the ray approximation to the heterogeneous Green’s function, accounts for acoustic absorption and dispersion. However, in practical scenarios, the absorption coefficient α_0 map and the exponent power y are typically unknown. In this study, the exponent power was assumed known and set to $y = 1.4$. Reconstructions were performed under three assumptions: (1) a known α_0 map (Figure 2(b)), (2) zero α_0 , and (3) a homogeneous α_0 within the breast. In practical scenarios, for each frequency subproblem, a rough homogeneous estimate of $\alpha = \alpha_0 \omega^y$ can be derived from the mean logarithmic relative amplitudes of the measured time series for only-water to breast-in-water datasets. (Here, the homogeneous absorption coefficient was heuristically set to $0.5 \text{ dBMHz}^{-y} \text{ cm}^{-1}$.)

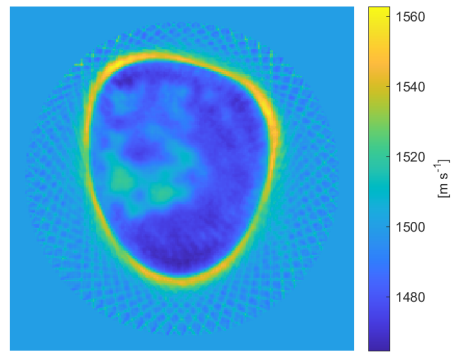
Figures 5(c) and 5(d) show the reconstructed sound speed images using the Hessian-based and Hessian-free ray-Born inversion approaches, respectively, under the assumption of a known heterogeneous α_0 map. Similarly, Figures 5(e) and 5(f) present reconstructions assuming $\alpha_0 = 0$, neglecting acoustic absorption and dispersion. Figures 5(g) and 5(h) show reconstructions assuming a homogeneous $\alpha_0 = 0.5 \text{ dBMHz}^{-y} \text{ cm}^{-1}$ within the breast. The RE values for these reconstructed images are provided in Table 1.

As seen in the figures, for high-SNR data, the Hessian-based approach, which implicitly and iteratively inverts the full Hessian matrix, yields more accurate reconstructions in terms of RE compared

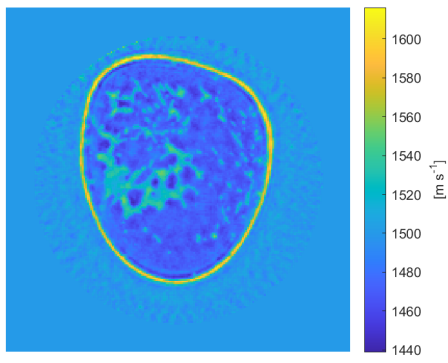
to the Hessian-free approach. This outcome is expected, as the approximations used in the Hessian-free method to diagonalize the Hessian matrix, as per Eqs. (30) and (31), trade off computational efficiency for slight accuracy degradation. Furthermore, for both inversion methods, assuming zero α_0 leads to less accurate images with more artifacts. However, assuming a homogeneous α_0 within the breast significantly improves image quality and reduces RE compared to the zero α_0 assumption. Finally, it should be emphasized that in all these experiments, the exponent power y was assumed to be known and fixed.



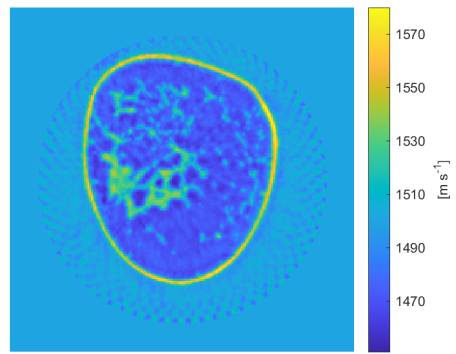
(a)



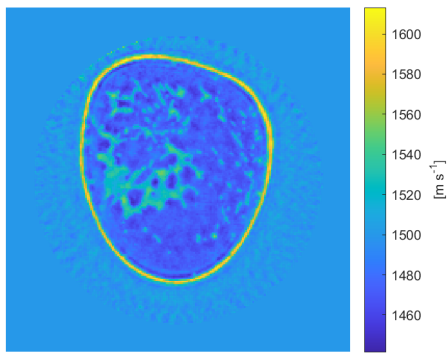
(b)



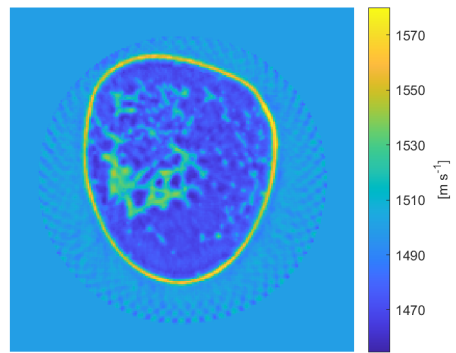
(c)



(d)



(e)



(f)

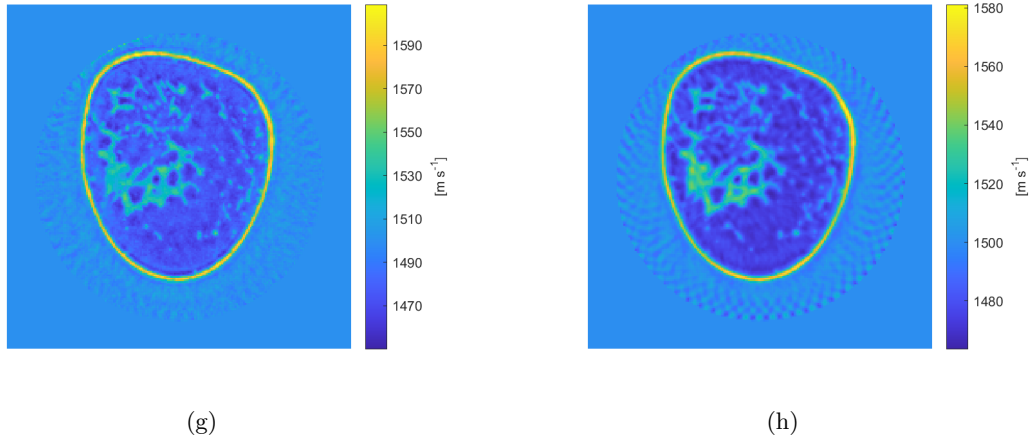


FIGURE 5. (a) Ground truth. Reconstructed sound speed images from UST data with 40 dB SNR: (b) Time-of-flight-based approach (initial guess). For the true α_0 (Figure 2(b)): (c) Hessian-based, (d) Hessian-free. For $\alpha_0 = 0$: (e) Hessian-based, (f) Hessian-free. For $\alpha_0 = 0.5 \text{ dB MHz}^{-y} \text{ cm}^{-1}$ (homogeneous within the breast): (g) Hessian-based, (h) Hessian-free. The colorbar range was adjusted to match the minimum and maximum sound speeds.

TABLE 1. Relative Error (RE) values (%) for reconstructed images at different SNR levels and assumptions for α_0 .

SNR (dB)	α_0 Assumption	Reconstruction Approach (RE %)		
		Time-of-Flight	Hessian-based	Hessian-free
40	Heterogeneous	73.35	38.69	42.92
	Zero	-	40.00	46.40
	Homogeneous	-	38.93	43.22
30	Heterogeneous	76.84	45.36	44.22
	Zero	-	47.19	49.24
	Homogeneous	-	46.30	45.09
25	Heterogeneous	81.04	54.20	46.55
	Zero	-	55.29	51.71
	Homogeneous	-	55.04	46.80

6.4.2. *Reconstructed images from UST data with medium and low SNR.* This section presents the sound speed images reconstructed from synthetic ultrasound data with 30 dB and 25 dB SNR, shown in figures 6 and 7, respectively. Similar to the high SNR case, the reconstructions were performed using the three assumptions for α_0 , and the results are displayed in the same format as figure 5. The corresponding RE values are summarized in Table 1.

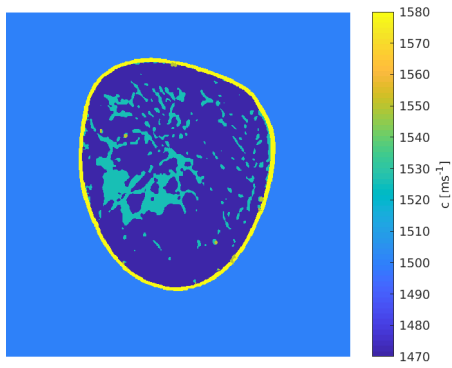
As observed in these figures, the images reconstructed using the Hessian-based inversion approach degraded more rapidly with decreasing SNR compared to those reconstructed using the Hessian-free approach, exhibiting more artifacts. This suggests that the Hessian-free method demonstrates improved robustness against variations in SNR.

The RE values in Table 1 further support this observation, showing that the Hessian-free approach maintains better stability under noise. Notably, while the reconstructed sound speed images degrade when assuming zero α_0 , assuming a homogeneous α_0 within the breast yields images with RE values comparable to those obtained with the heterogeneous true α_0 . This indicates that the homogeneous α_0 assumption aligns well with the approximations in (30) and (31), which are used to diagonalize the Hessian matrix in the Hessian-free method.

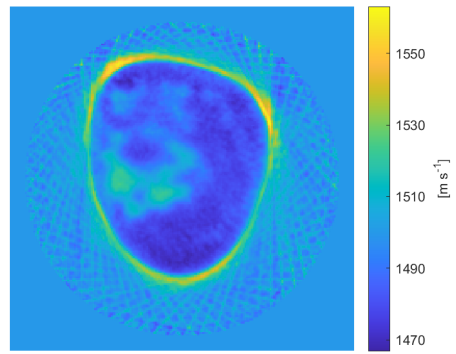
6.5. Reconstructed sound speed profiles. Figures 8(a), 8(b), and 8(c) display the reconstructed sound speed profiles along $x = 0$, the horizontal middle line of the image reconstruction domain, for UST data with SNR values of 40 dB, 30 dB, and 25 dB, respectively. The true sound speed values for the digital breast phantom are plotted in black, while those obtained using the TOF-based approach are shown in green. Sound speed profiles reconstructed using the Hessian-based method are presented in blue, and those reconstructed using the proposed Hessian-free inversion approach are shown in red. To highlight the avoidance of inverse crime, the true phantom values are sampled on the grid used for data simulation rather than the reconstruction grid.

As seen in these figures, the Hessian-free approach effectively reconstructs sharp sound speed variations associated with small anomalies, albeit with slightly reduced contrast compared to the Hessian-based method. Nonetheless, the Hessian-free reconstructions demonstrate superior stability against data noise relative to the Hessian-based approach. This enhanced stability is attributed to the regularization effects arising from the approximations employed in diagonalizing the Hessian matrix (Eqs. (30) and (31)).

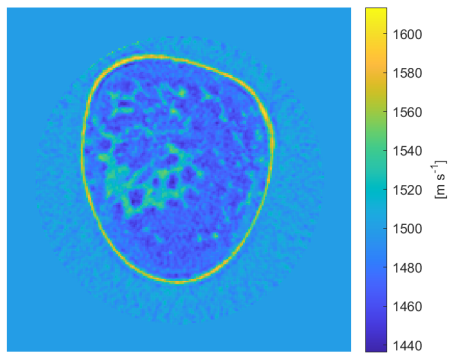
Furthermore, it is important to note that the computational cost of the proposed Hessian-free inversion approach is nearly an order of magnitude lower than that of the Hessian-based method, as each linearized subproblem is solved in a single step.



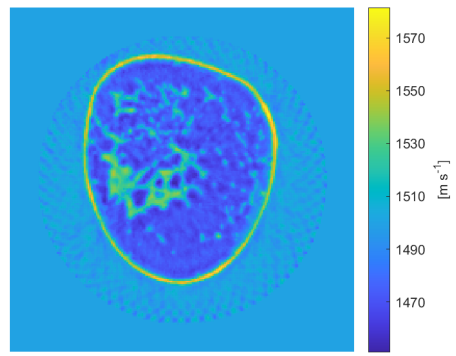
(a)



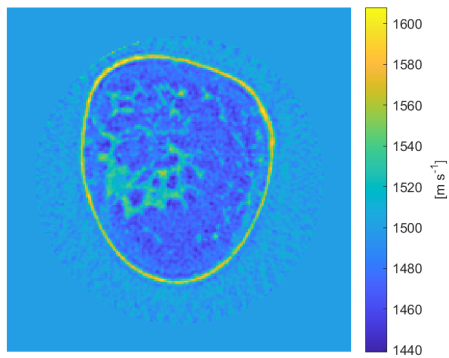
(b)



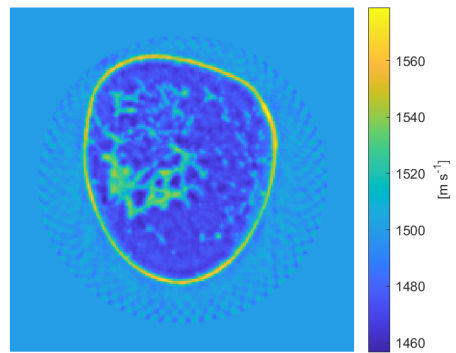
(c)



(d)



(e)



(f)

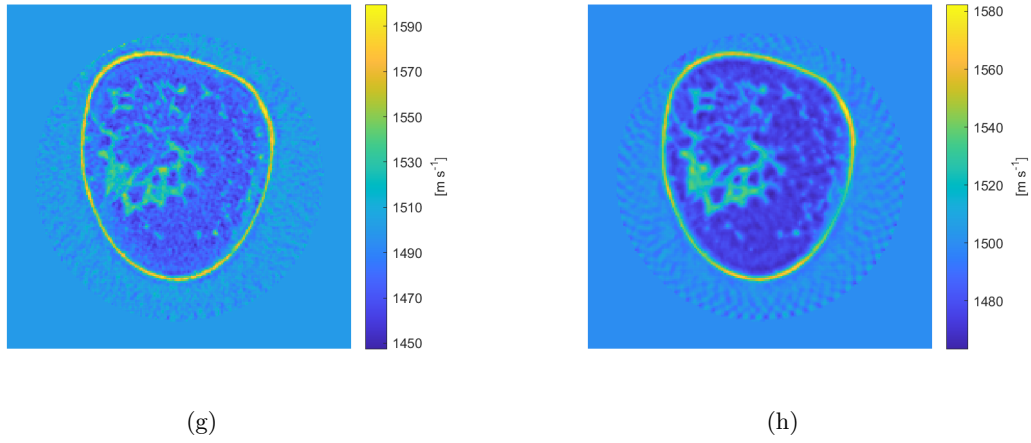
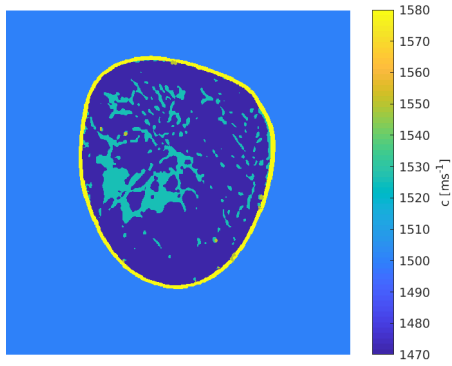
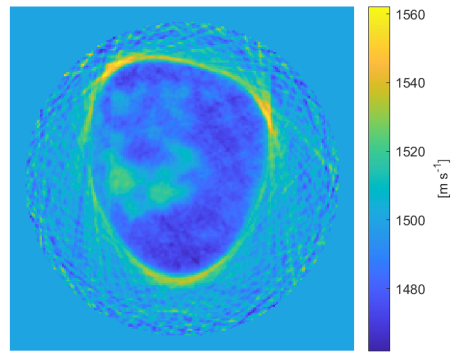


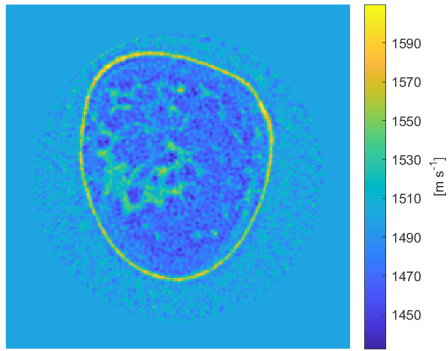
FIGURE 6. (a) Ground truth. Reconstructed sound speed images from UST data with 30 dB SNR: (b) Time-of-flight-based approach (initial guess). For the true α_0 (Figure 2(b)): (c) Hessian-based, (d) Hessian-free. For $\alpha_0 = 0$: (e) Hessian-based, (f) Hessian-free. For $\alpha_0 = 0.5 \text{ dB MHz}^{-y} \text{ cm}^{-1}$ (homogeneous within the breast): (g) Hessian-based, (h) Hessian-free. The colorbar range was adjusted to match the minimum and maximum sound speeds.



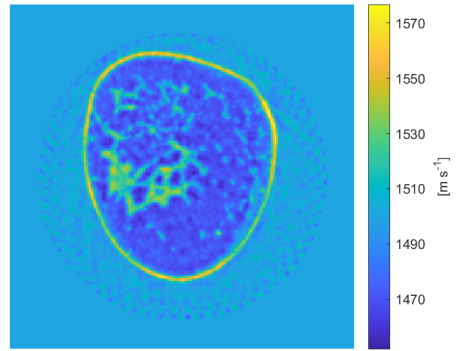
(a)



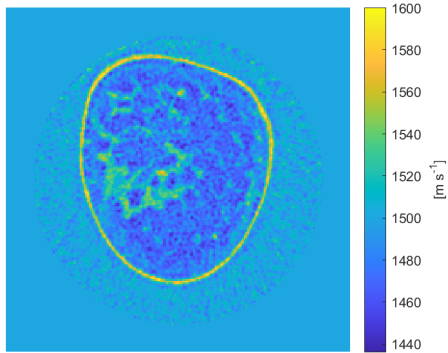
(b)



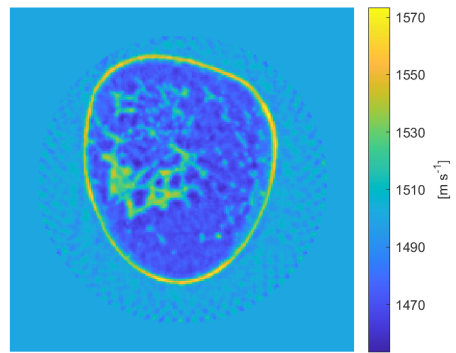
(c)



(d)



(e)



(f)

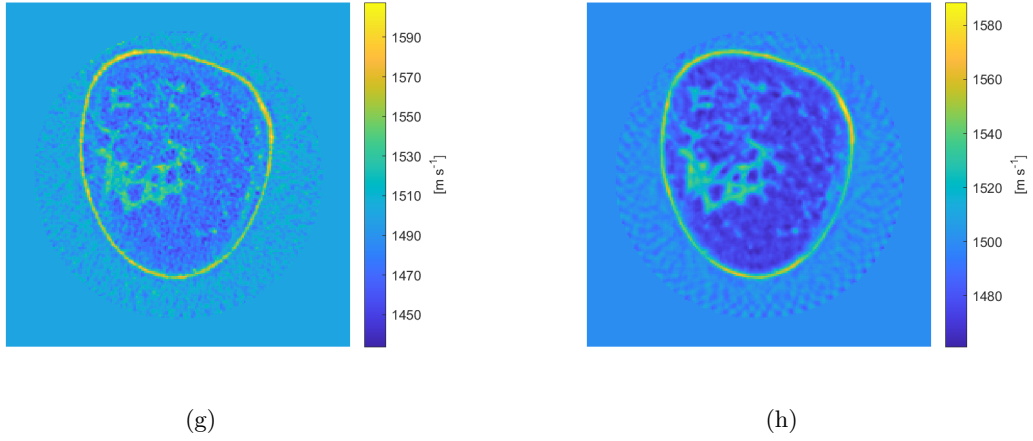
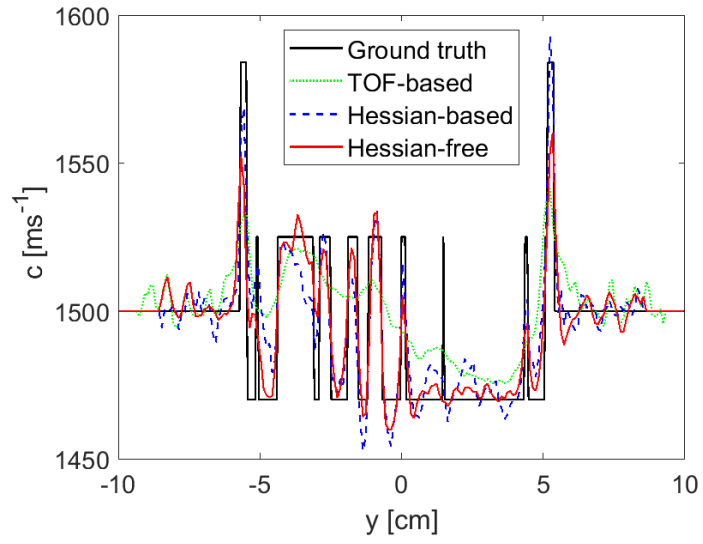
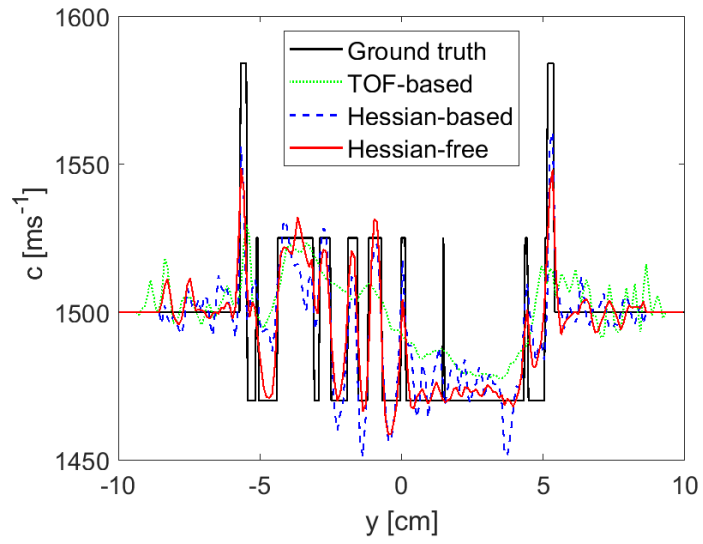


FIGURE 7. (a) Ground truth. Reconstructed sound speed images from UST data with 25 dB SNR: (b) Time-of-flight-based approach (initial guess). For the true α_0 (Figure 2(b)): (c) Hessian-based, (d) Hessian-free. For $\alpha_0 = 0$: (e) Hessian-based, (f) Hessian-free. For $\alpha_0 = 0.5 \text{ dB MHz}^{-y} \text{ cm}^{-1}$ (homogeneous within the breast): (g) Hessian-based, (h) Hessian-free. The colorbar range was adjusted to match the minimum and maximum sound speeds.



(a)



(b)

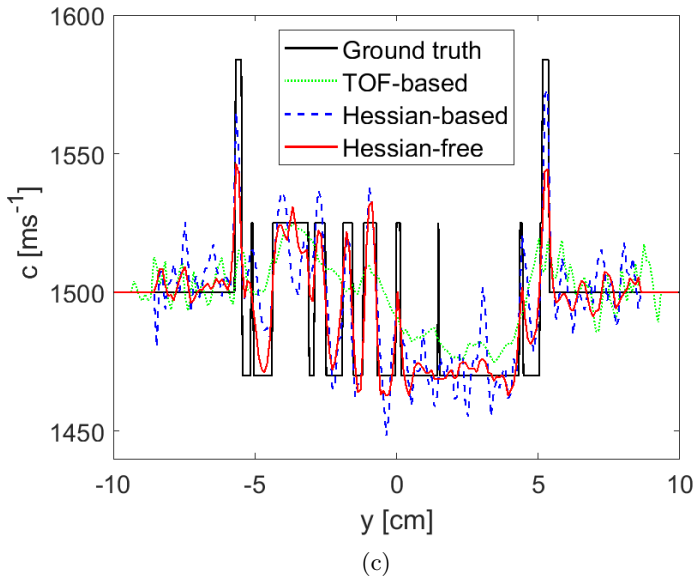


FIGURE 8. The sound speed values along $x = 0$ with: a) 40 dB, b) 30 dB and c) 25 dB synthetic data.

7. DISCUSSION AND CONCLUSION

This manuscript proposed a robust and computationally efficient approach for quantitatively reconstructing sound speed from transmission ultrasound time series. It demonstrated the ability to generate high-resolution and quantitatively accurate images of the sound speed in soft tissues. The proposed image reconstruction method was validated using a realistic digital breast phantom [45]. Similar to the inversion approach proposed in [1], the propagation of acoustic waves was modeled using Green’s formula, which accounts for aberrations in the phase and amplitude of the Green’s function caused by heterogeneity, refraction, geometrical spreading, and acoustic absorption and dispersion. Geometrical spreading losses were approximated by computing changes in the ray tube area for each linked ray via solving the paraxial system of equations as described in Section 4. The proposed ray-based inversion method achieved high-resolution imaging of the breast phantom by including first-order scattered waves in the reconstruction. In practical settings, higher-order scattered waves are often attenuated due to acoustic absorption or buried in noise.

This approach represents a significant improvement over prototype Born and distorted Born inversion techniques used in medical UST, which neglect medium heterogeneity in modeling the Green’s function and incorporate it only in the scattering potential [15, 16, 17, 18, 19, 20, 22, 23, 24, 25]. As illustrated in Figures 4(a) and 4(b), disregarding acoustic heterogeneities when computing the Green’s function results in substantial errors in phase and amplitude approximations, respectively. The computational cost of the Hessian-based inversion approach in [1], which solves each linearized frequency subproblem iteratively via implicit inversion of the Hessian matrix, is low and comparable to a single iteration of a full-waveform inversion approach [35].

To further reduce the computational burden, this study introduced a Hessian-free inversion method that is approximately an order of magnitude faster than the Hessian-based approach. This efficiency is achieved by solving each linearized subproblem in a single step using Eqs. (44) and (45).

The approximations (30) and (31) not only facilitate the inversion of the Hessian matrix in a single step but also introduce regularization effects and enhance stability against noise, producing reconstructed images with fewer artifacts than the Hessian-based approach for UST data with SNR values of 30 dB and 25 dB. Additionally, the Hessian-free method exhibited reduced sensitivity to variations in reconstruction parameters or the initial guess, further highlighting its robustness.

The proposed forward model incorporates acoustic absorption and dispersion by solving a lossy Helmholtz equation based on Szabo’s wave model. Since absorption coefficient maps are typically unknown in practice, this study demonstrated that assuming a homogeneous absorption coefficient within the breast produced images comparable to those obtained using a true absorption map, whereas neglecting absorption entirely resulted in less accurate reconstructions.

Ray-Born inversion approaches typically combine ray theory with the Born approximation. The latter assumes that, for each emitter-receiver pair, scattered waves measured at the receiver can originate from any point within the medium. Alternatively, the proposed inversion method adopts a high-frequency approximation, assuming that waves scatter more likely near the ray connecting the emitter-receiver pair than from regions farther away. While this assumption is not exact, it holds well for the frequency ranges employed in prototype ultrasound systems [3, 5].

The diagonalization of the Hessian matrix relies on an exact 2D Fourier integral of the Dirac delta function. However, due to the inherently band-limited nature of transducers, the coverage of $|\bar{\mathbf{k}}|$ is partial, necessitating an approximation of the Fourier integral. This approximation results in a smoothed Dirac delta function in space. While this smoothing slightly reduces image contrast and resolution, as shown in Figures 8(a), 8(b), and 8(c), it substantially improves reconstruction stability by mitigating the effects of noise, variations in initial guesses, and reconstruction parameters. It is anticipated that the use of more broadband transducers could further enhance spatial resolution and contrast, particularly when employing the Hessian-free approach.

The primary motivation for developing this image reconstruction approach and the ray-based methods in [1, 36] lies in their potential application to volumetric reconstruction from 3D UST data. Acoustic waves naturally propagate in three dimensions rather than being confined to a horizontal plane. While full-waveform approaches offer numerous well-known advantages, they face significant limitations in terms of computational cost and the ability to handle transducer directivity in specific 3D configurations, particularly when transducers are of finite size. These challenges can be addressed more effectively using ray-based methods.

Considering that this study employed distinct methodologies for simulating synthetic UST data and reconstructing images, the findings highlight the potential for effective translation to practical 2D and 3D applications. Preliminary experimental results further validate the successful adaptation of this approach to experimental settings, with these outcomes to be detailed in future studies.

DATA AND CODE AVAILABILITY STATEMENT

The MATLAB codes supporting the findings of this study, as well as those reported in [1] and [36], are publicly accessible via the GitHub repository referenced in [47]. The original k-Wave simulated ultrasound data [35], used as a benchmark in this study (after applying the modification reported in Section 6.1 of [49]), can be reproduced using the example scripts provided in [47] or downloaded directly from the Zenodo repository referenced in [48]. To utilize the data, users should add the downloaded files to the appropriate paths.

RESEARCH INTEGRITY

In compliance with UCL’s Principles of Research Integrity, the k-Wave toolbox [35] was modified to incorporate point sources in terms of s , as emitters were assumed to be point sources in this

study. This modification was carried out in accordance with the guidelines outlined in Section 6.1 of [49], ensuring both methodological rigor and consistency. The modification has been consistently documented throughout the manuscript to uphold transparency and integrity in the research process.

DECLARATION OF INTERESTS

The author declares no known competing financial interests or personal relationships that could have influenced the work reported in this paper.

ACKNOWLEDGMENTS

This work was predominantly conducted at the Department of Medical Physics and Biomedical Engineering, University College London, UK, during the author's employment there. The project was funded by the UK EPSRC Grant under Project Reference: EP/T014369/1. Subsequent refinements and revisions were completed at the University of Tehran.

APPENDIX A: EIKONAL AND TRANSPORT EQUATIONS

This appendix outlines the derivation of the Eikonal equation (10) and the Transport equation (11). Substituting the Green's function (9) into the wave equation (8), along with the complex wavenumber defined by (4), yields the following system of equations:

$$\begin{aligned} k^2 A + \nabla^2 A - A \nabla \phi \cdot \nabla \phi &= 0, \\ 2k\alpha A + 2\nabla A \cdot \nabla \phi + A \nabla^2 \phi &= 0, \end{aligned} \quad (65)$$

where the first equation corresponds to the real part, and the second equation corresponds to the imaginary part. Here, we have used the approximation $\tilde{k}^2 \approx k^2 + 2\alpha k i$.

Applying the high-frequency approximation, $|\nabla^2 A/A| \ll k^2$, the first equation simplifies to the dispersive Eikonal equation (10), which determines the rays' trajectories as tangents to the complex wavevector $\mathbf{k} = \nabla \phi$. For the second equation, introducing $A = A_{abs} A_{geom}$, where A_{abs} satisfies (14), leads to:

$$2k\alpha A_{geom} + 2\nabla A_{geom} \cdot \nabla \phi - 2A_{geom} \frac{\alpha}{k} \mathbf{k} \cdot \nabla \phi + A_{geom} \nabla^2 \phi = 0, \quad (66)$$

where the relation $\nabla A_{abs} = -[\alpha/k] \mathbf{k} A_{abs}$ has been applied. Substituting $\mathbf{k} = \nabla \phi$ into the above equation yields the Transport equation (11).

APPENDIX B: HOMOGENEOUS GREEN'S FUNCTION

This appendix presents the Green's functions for homogeneous media. For a 2D homogeneous medium, the Green's function is given as [1]:

$$g_{0,2D}(\omega, \mathbf{x}, \mathbf{x}') \approx [8\pi\phi_0(\omega, \mathbf{x}, \mathbf{x}')]^{-1/2} \exp\left(i[\phi_0(\omega, \mathbf{x}, \mathbf{x}') + \pi/4]\right). \quad (67)$$

For a 3D homogeneous medium, the Green's function is expressed as [1]:

$$g_{0,3D}(\omega, \mathbf{x}, \mathbf{x}') = [4\pi|\mathbf{x} - \mathbf{x}'|]^{-1} \exp\left(i\phi_0(\omega, \mathbf{x}, \mathbf{x}')\right). \quad (68)$$

As noted above, $\phi_0(\omega, \mathbf{x}, \mathbf{x}') = k_0|\mathbf{x} - \mathbf{x}'|$ represents the accumulated phase, with $k_0 = \omega/c_0$ denoting the wavenumber in water.

REFERENCES

- [1] A. Javaherian and B. Cox, Ray-based inversion accounting for scattering for biomedical ultrasound tomography, *Inverse Problems* vol. 37, no.11, 115003, 2021.
- [2] J. F. Synnevag, A. Austeng and S. Holm, Adaptive beamforming applied to medical ultrasound imaging, *IEEE transactions on ultrasonics, ferroelectrics, and frequency control*, Vol. 54, no. 8, pp. 1606-1613, 2007. DOI: 10.1109/TUFFC.2007.431.
- [3] N. Duric P. Littrup, L. Poulo, A. Babkin, R. Pevzner, E. Holsapple, O. Rama and C. Glide, Detection of breast cancer with ultrasound tomography: First results with the Computed Ultrasound Risk Evaluation (CURE) prototype, *Med. Phys.* vol. 34, no.2, 2007.
- [4] N. V. Ruiter, M. Zapf, T. Hopp, R. Dapp, E. Kretzek, M. Birk, B. Kohout, H Gemmeke, 3D ultrasound computer tomography of the breast: A new era?, *European Journal of Radiology*, vol. 81, Supplement 1, pp. S133-S134, 2012.
- [5] H. Gemmeke, T. Hopp, M. Zapf, C. Kaiser, N.V. Ruiter, 3D Ultrasound Computer Tomography: Hardware Setup, Reconstruction Methods and First Clinical Results, *NUCL INSTRUM METH A*, vol. 873, 2017, pp. 59-65, 2017.
- [6] T. Hopp, N. Ruiter, J. C. Bamber, N. Duric and K.W.A. van Dongen (Eds.) 2017 International Workshop on Medical Ultrasound Tomography, Speyer, Germany.
- [7] C. Li, N. Duric, P. Littrup and L. Huang, In-vivo breast sound speed imaging with ultrasound computed tomography, *Ultrasound in Med. & Biol.*, vol. 35, no. 10, pp. 1615–1628, 2009.
- [8] C. Li, L. Huang, N. Duric, H. Zhang, and C. Rowe, An improved automatic time-of-flight picker for medical ultrasound tomography, *Ultrasonics.*, vol. 49, pp. 61-72, 2009.
- [9] K. J. Opielinski, P. Pruchnicki, P. Szymanowski, W. K. Szeplieniec, H. Szweda, E. Swis, M. Jozwik, M. Tenderenda and M. Bułkowskif, Multimodal ultrasound computer-assisted tomography: An approach to the recognition of breast lesions, *COMPUT MED IMAG GRAP* vol. 65, pp. 102–114, 2018.
- [10] G. Y. Sandhu, C. Li, O. Roy, S. Schmidt, and N. Duric, Frequency domain ultrasound waveform tomography: breast imaging using a ring transducer, *Phys. Med. Biol.*, Vol. 60, 5381–5398, 2015.
- [11] J. W. Wiskin, D. T. Borup, E. Iuanow, J. Klock, M. W. Lenox, 3-D Nonlinear Acoustic Inverse Scattering: Algorithm and Quantitative Results, *IEEE T ULTRASON FERR*, vol. 64, no. 3, 2017.
- [12] A. V. Goncharsky and S. Y. Romanov, Iterative methods for solving coefficient inverse problems of wave tomography in models with attenuation, *Inverse Problems*, vol. 33, pp. 025003, 2017.
- [13] S. Bernard , V. Monteiller , D. Komatitsch and P. Lasaygues, Ultrasonic computed tomography based on full-waveform inversion for bone quantitative imaging, *Phys. Med. Biol.* Vol. 62, pp. 7011–7035, 2017.
- [14] R. Ali, T. M. Mitcham, T. Brevett, Ò. Calderón Agudo, C. Durán Martinez, C. Li, M. M. Doyley and N. Duric., "2-D Slicewise Waveform Inversion of Sound Speed and Acoustic Attenuation for Ring Array Ultrasound Tomography Based on a Block LU Solver," in *IEEE Trans. Med. Imag.*, doi: 10.1109/TMI.2024.3383816.
- [15] A. J. Devaney, A filtered backpropagation algorithm for diffraction tomography, *Ultrason. Imag.*, vol. 4, pp. 336–350, 1982.
- [16] A. J. Devaney and M. L. Oristaglio, Inversion procedure for inverse scattering within the distorted-wave Born approximation, *Physical Review Letters*, vol. (51), no. 4, 1983.
- [17] W. B. Beydoun and A. Tarantola, First Born and Rytov approximations: Modelling and inversion conditions in a canonical example, *J. Acoust. Soc. Am.*, vol. 83, pp. 1045-1055, 1988.
- [18] D. T. Borup, S. A. Johnson, W. W. Kimz and M. J. Berggren, Nonperturbative Diffraction tomography via Gauss-Newton iteration applied to the scattering integral equation, *Ultrasonic Imaging*, vol. 14, pp. 69-85, 1992.
- [19] T.D. Mast, Aberration correction for time-domain ultrasound diffraction tomography, *J. Acoust. Soc. Am.*, vol. 112, No. 1, 2002.
- [20] F. Simonetti, L. Huang, N. Duric, and P. Littrup, Diffraction and coherence in breast ultrasound tomography: A study with a toroidal array, *Med. Phys.*, vol. 36, pp. 2955, 2009.
- [21] P. Müller, M. Schürmann, and J. Guck, ODTbrain: a Python library for full-view, dense diffraction tomography, *BMC Bioinformatics*, Vol. 16, p. 367, 2015.
- [22] N. K. Martiartu, C. Boehm and A. Fichtner, 3-D Wave-Equation-Based Finite-Frequency Tomography for Ultrasound Computed Tomography, *IEEE Transactions on Ultrasonics, Ferroelectrics, and Frequency Control*, Vol. 67, no. 7, pp. 1332 - 1343, 2020.
- [23] Y. Fan and L. Ying, Solving inverse wave scattering with deep learning, *Annals of Mathematical Sciences and Applications*, Vol. 7, No. 1, pp. 23–48, 2022.

- [24] F. Faucher, C. Kirisits, M. Quellmalz, O. Scherzer and E. Setterqvist, Diffraction Tomography, Fourier Reconstruction, and Full Waveform Inversion, In Handbook of Mathematical Models and Algorithms in Computer Vision and Imaging, 2022, doi. 10.1007/978-3-030-03009-4.
- [25] Y. Guo, H. Li and X. Wang, A novel time-domain direct sampling approach for inverse scattering problems in acoustics, , Vol. 84, no. 5, pp. 2152-2174, 2024.
- [26] P. Thierry, S. Operto, and G. Lambare, Fast 2-D ray+Born migration/inversion in complex media, *Geophysics*, Vol. 64, No. 1, pp. 162–181, 1999.
- [27] V. Červený, Seismic ray theory, Cambridge University Press. 2001.
- [28] P. Huthwaite and F. Simonetti, High-resolution imaging without iteration: a fast and robust method for breast ultrasound tomography, *J. Acoust. Soc. Am.*, vol. 130, no. 3, pp. 1721-34, 2011.
- [29] S. Jin, R. Madariaga, J. Virieux, and G. Lambaré, Two-dimensional asymptotic iterative elastic inversion, *Geophys. J. Internat.*, Vol. 108, No.2, pp. 575–588, 1992.
- [30] G. Lambare, J. Virieux, R. Madariaga, and S. Jin, Iterative asymptotic inversion in the acoustic approximation, *Geophysics*, Vol. 57. No. 9, pp. 1138-1154, 1992.
- [31] G. Lambare, S. Operto, P. Podvin, and P. Thierry, 3D ray+Born migration/inversion—Part 1: Theory, *Geophysics*, Vol. 68, No. 4, 2003.
- [32] N. N. Bojarski, The k-space formulation of the scattering problem in the time domain, *J. Acous. Soc. Am.*, vol. 72, 1982, pp. 570–584.
- [33] T. D. Mast, L. P. Souriau, D. D. Liu, M. Tabei, A. I. Nachman, and R. C. Waag, A k-space method for large-scale models of wave propagation in tissue, *IEEE Trans. Ultrason. Ferroelectr. Freq. Control*, vol. 48, 2001, pp. 341–354.
- [34] M. Tabei, T. D. Mast, and R. C. Waag, A k-space method for coupled first-order acoustic propagation equations *J. Acoust. Soc. Am.* vol. 111, pp. 53–63, 2002.
- [35] B. E. Treeby and B. T. Cox, k-Wave: MATLAB toolbox for the simulation and reconstruction of photoacoustic wave fields *J. Biomed. Opt.* vol. 15, no. 2, 021314, 2010.
- [36] A. Javaherian, F. Lucka and B. Cox, Refraction-corrected ray-based inversion for three-dimensional ultrasound tomography of the breast, *Inverse Problems*, vol. 36, 125010, 2020.
- [37] J. F. Kelly, R. J. McGough, and M. M. Meerschaert, Analytical time-domain Green’s functions for power-law media, *J. Acoust. Soc. Am.*, vol. 124, no. 5, pp. 2861–2872, 2008.
- [38] T. L. Szabo, Time domain wave equations for lossy media obeying a frequency power law, *J. Acoust. Soc. Am.*, vol. 96, pp. 491–500, 1994.
- [39] M. Liebler, S. Ginter, T. Dreyer, and R. E. Riedlinger, “Full wave modeling of therapeutic ultrasound: Efficient time-domain implementation of the frequency power-law attenuation, *J. Acoust. Soc. Am.*, vol. 116, pp. 2742–2750, 2004.
- [40] A. D. Pierce, 1981 Acoustics: An Introduction to its Physical Principles and Applications 3rd Edition (Berlin: Springer and ASA Press) (<https://doi.org/10.1007/978-3-030-11214-1>)
- [41] J. Virieux and V. Ferra Ray tracing in 3D complex isotropic media: An analysis of the problem, *Geophysics*, vol. 56, no. 12, pp. 2057-2069, 1991.
- [42] F. Rul-lan and M. M. Betcke, Hamilton-Green solver for the forward and adjoint problems in photoacoustic tomography, *J. Comput. Phys.*, Vol. 449, 2022, pp. 110797.
- [43] J.C. Butcher, The numerical analysis of ordinary differential equations. Runge–Kutta and general linear methods, Wiley, 1987.
- [44] E. Kreyszig, 1993 Advanced Engineering Mathematics. John Wiley & Sons, Inc., New York.
- [45] Y. Lou, W. Zhou, T. P. Matthews, C. M. Appleton and M. A. Anastasio, Generation of anatomically realistic numerical phantoms for photoacoustic and ultrasonic breast imaging, *J Biomed Opt.*, vol. 22, no. 4, pp. 041015, 2017.
- [46] A. H. Anderson and A.C. Kak, Simultaneous algebraic reconstruction techniques (SART): A superior implementation of the ART algorithm, *Ultrasonic Imaging*, vol. 6, no. 1, pp. 81-94, 1984.
- [47] Ashkan Javaherian, Ray-based quantitative ultrasound-tomography toolbox, 2022, <https://github.com/Ash1362/ray-based-quantitative-ultrasound-tomography/>
- [48] Ashkan Javaherian, Transmission ultrasound data simulated using the k-Wave toolbox as a benchmark for biomedical quantitative ultrasound tomography using a ray approximation to Green’s function, 2023, <https://zenodo.org/records/7717290>
- [49] Ashkan Javaherian and Seyed Kamaledin Setarehdan, Forward and Time-Reversed Full-Field Approximation for Finite-Size Acoustic Apertures, 2022 (v1)- 2024 (v14), <https://arxiv.org/abs/2212.04466>.